APPENDICES

Appendix - I

Phytochemical screening (Harbone, 1973)

Detection of alkaloids: Extracts were dissolved individually in dilute Hydrochloric acid and filtered.

- **Dragendroff's Test:** Filtrates were treated with Dragendroff's reagent (solution of Potassium Bismuth Iodide). Formation of a red precipitate indicates the presence of alkaloids.

- **Hager's Test:** Filtrates were treated with Hager's reagent (saturated picric acid solution). Presence of alkaloids confirmed by the formation of a yellow colour precipitate.

Detection of carbohydrates: Extracts were dissolved individually in 5 ml distilled water and filtered. The filtrates were used to test for the presence of carbohydrates.

- **Molisch's Test:** Filtrates were treated with 2 drops of alcoholic α-naphthol solution in a test tube. Formation of the violet ring at the junction indicates the presence of Carbohydrates.

- **Benedict's test:** Filtrates were treated with Benedict's reagent and heated gently. Orange-red precipitate indicates the presence of reducing sugars.

Detection of saponins:

- **Froth Test:** Extracts were diluted with distilled water to 20ml and this was shaken in a graduated cylinder for 15 minutes. Formation of a 1 cm layer of foam indicates the presence of saponins.

- **Foam Test:** 0.5 gram of the extract was shaken with 2 ml of water. If foam produced persists for ten minutes it indicates the presence of saponins.

Detection of phenols:

- **Ferric Chloride Test:** Extracts were treated with 3-4 drops of ferric chloride solution. Formation of bluish-black colour indicates the presence of phenols.

Detection of tannins:

- **Gelatin Test:** To the extract, 1% gelatin solution containing sodium chloride was added. Formation of a white precipitate indicates the presence of tannins.

Detection of flavonoids:

- **Alkaline Reagent Test:** Extracts were treated with a few drops of sodium hydroxide solution. Formation of intense yellow colour, which becomes colourless on the addition of dilute acid, indicates the presence of flavonoids.

- **Lead acetate Test:** Extracts were treated with a few drops of lead acetate solution. Formation of a yellow colour precipitate indicates the presence of flavonoids.

Detection of Steroids:

- **Libermann buchard test:** Extracts were treated with few drops of Glacial Acetic acid to the filtrate, warm for 15 minutes, cool and add 1ml of Concentrated Sulphuric acid. The formation of a brown ring at the junction of two layers indicates the presence of steroids.

Detection of Reducing sugar:

- **Fehling's test:** Extracts were treated with a few drops of Fehling's solution, warm for 15 minutes. The formation of reddish-brown colour indicates the presence of reducing sugar.

Detection of Terpenoids:

- **Salkowski's test:** Extracts were treated with few drops of 2ml of Chloroform and 3ml of Concentrated Sulphuric acid. The formation of reddish-brown colour indicates the presence of Terpenoids.

- **Detection of Quinones:** Extracts were treated with few drops of Conc. sulphuric acid was added. A formation of red colour indicates the presence of Quinones.

Appendix-II

GCD Profiles of SPL/TCL/SN/TN

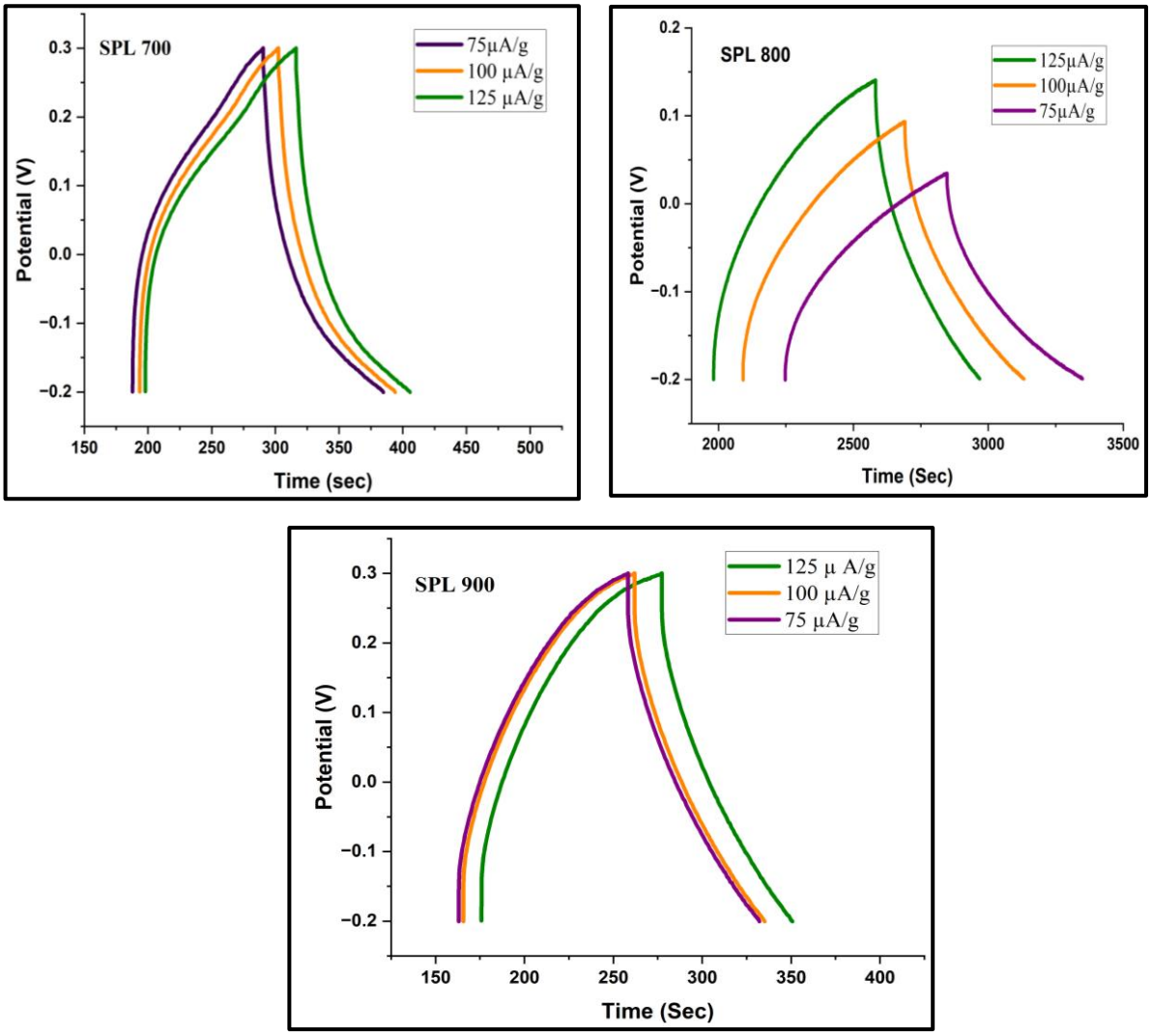

Figure A1: GCD Profiles for SPL 700, SPL 800, SPL 900 at current density of 75µA/g, 100 µA/g and 125 µA/g

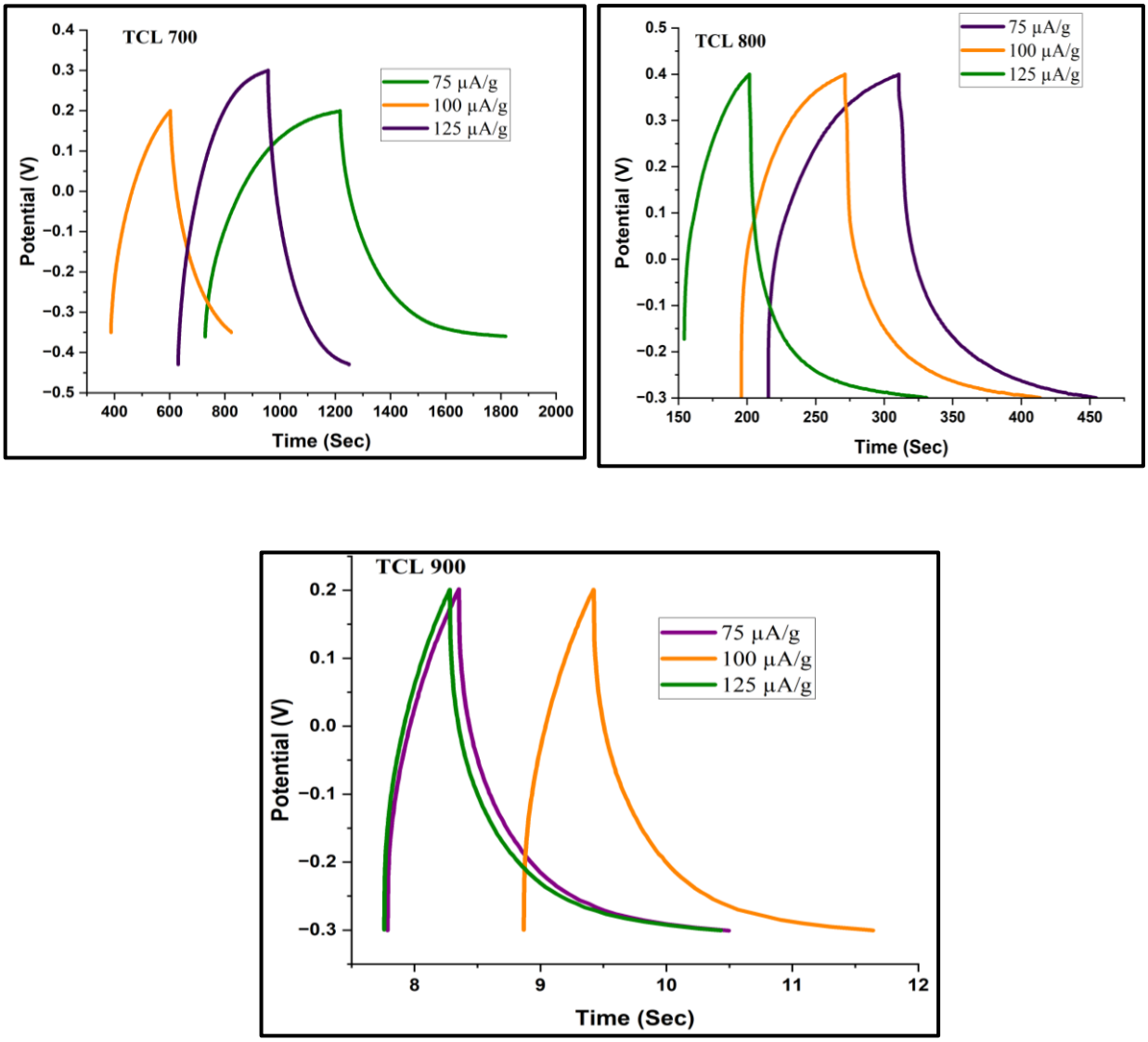

Figure A2: GCD Profiles for TCL 700, TCL 800, TCL 900 at current density of 75µA/g, 100 µA/g and 125 µA/g

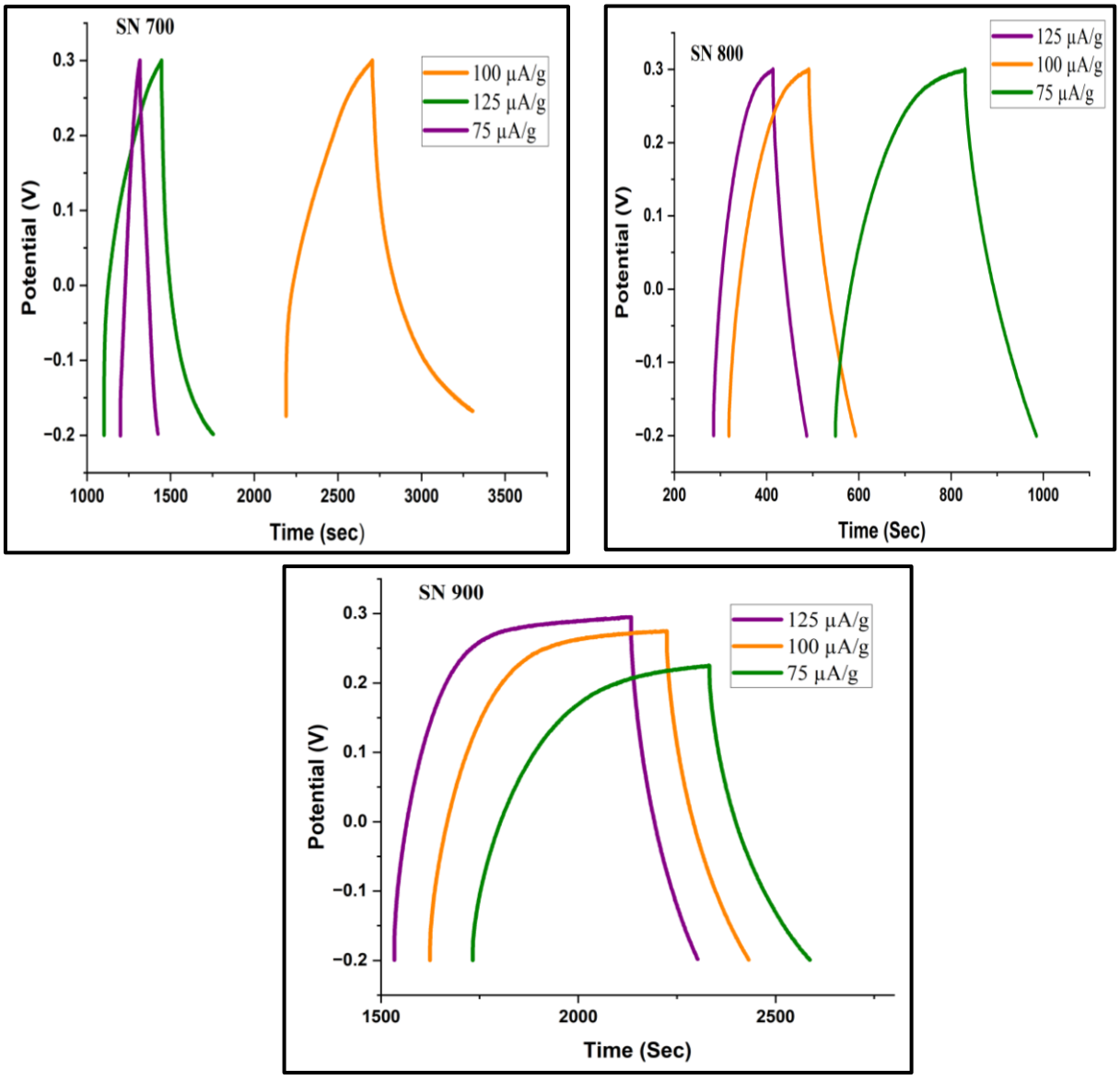

Figure A3: GCD Profiles for SN 700, SN 800, SN 900 at current density of 75µA/g, 100 µA/g and 125 µA/g

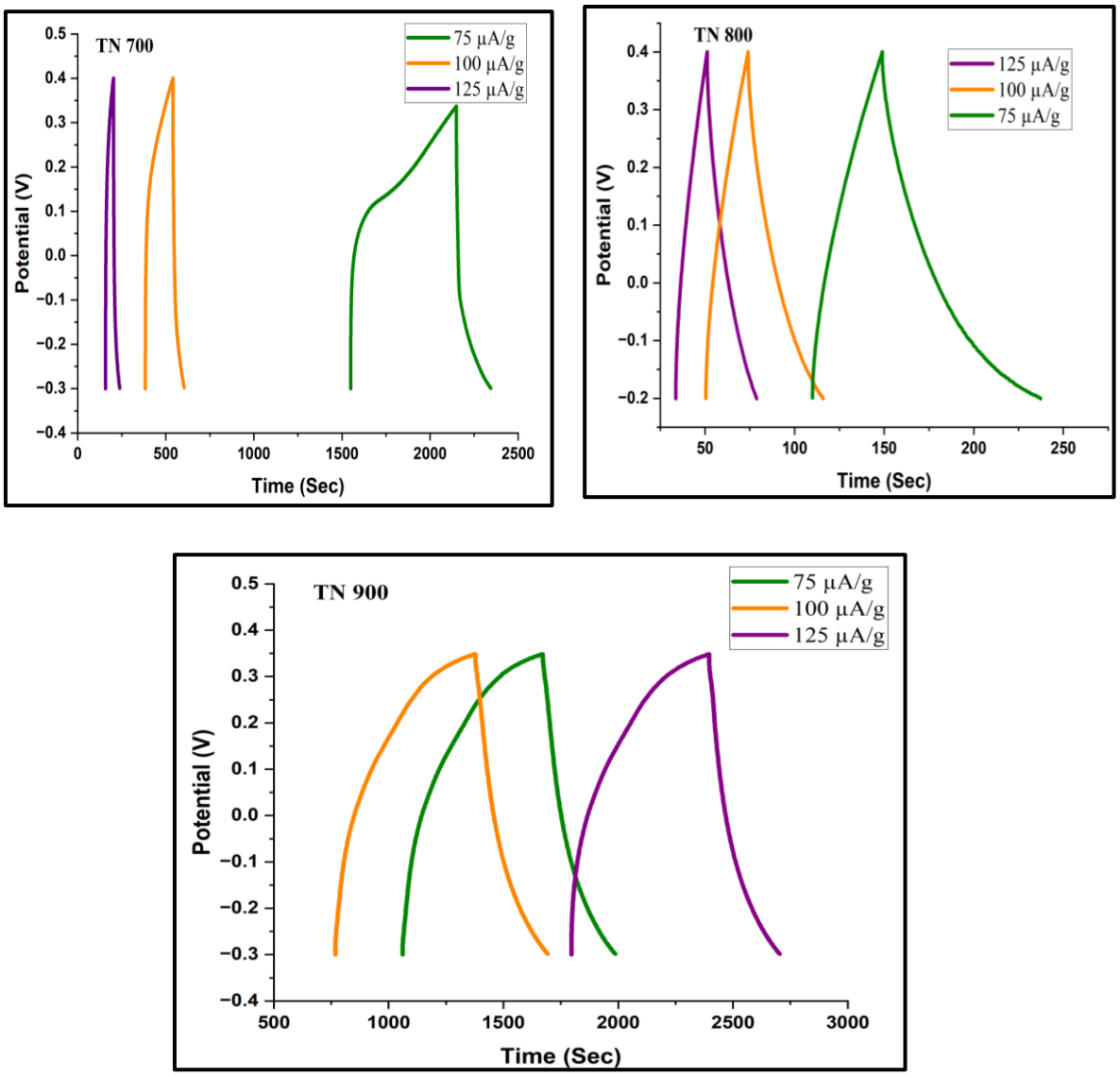

Figure A4: GCD Profiles for TN 700, TN 800, TN 900 at current density of 75µA/g, 100 µA/g and 125 µA/g

In galvanostatic charge/discharge experiments, the SPL/TCL/SN/TN 700 series demonstrates predominantly capacitive behavior at higher frequencies, transitioning to more resistive behavior at lower frequencies. Consequently, the initial response, driven by high-frequency characteristics, results in a potential increase at lower potentials.

भारतसरकार
GOVERNMENT OF INDIA
पर्यावरण,वनऔरजलवायुपरिवर्तनमंत्रालय
MINISTRY OF ENVIRONMENT, FOREST & CLIMATE CHANGE
भारतीयवनस्पतिसर्वेक्षण
BOTANICAL SURVEY OF INDIA

दक्षिणीक्षेत्रीयकेन्द्र / Southern Regional Centre
टी,एन.ए.यूकैम्पस/ T.N.A.U. Campus
लाउलीरोड/ Lawley Road
कोयंबत्तूर/ Coimbatore - 641 003

टेलीफोन / Phone: 0422-2432788, 2432123, 2432487
टेलीफक्स/ Telefax: 0422- 2432835
ई-मैल/E-mail id: sc@bsi.gov.in
bsisc@rediffmail.com

सं. भा.व.स./द.क्षे.के./No.: BSI/SRC/5/23/2022/Tech /497

दिनांक/Date: 22nd September 2022

पादप प्रमाणीकरण प्रमाणपत्र / PLANT AUTHENTICATION CERTIFICATE

The plant specimen brought by you for authentication is identified as ***Tecomaria capensis*** **(Thunb.) Spach - BIGNONIACEAE.**

अभिनिर्धारित प्रतिरूप को संबंधित कॉलेज/विभाग/संस्थान के पादपालय में परिरक्षण हेतु वापस किया जाता है।/ The identified specimen is returned herewith for preservation in their College/ Department/ Institution Herbarium.

22/9/2022

डॉ. एम. यु. शरीफ़/DR. M. U. SHARIEF
वैज्ञानिक 'एफ' एवं कार्यालयाध्यक्ष/
SCIENTIST 'F' & HEAD OF OFFICE

सेवा में / To

Ms. S. THARANI
Ph.D. Research Scholar
Department of Chemistry
Avinashilingam Institute for Home Science &
Higher Education for Women
COIMBATORE – 641 043

भारतसरकार
GOVERNMENT OF INDIA
पर्यावरण,वनऔरजलवायुपरिवर्तनमंत्रालय
MINISTRY OF ENVIRONMENT, FOREST & CLIMATE CHANGE
भारतीयवनस्पतिसर्वेक्षण
BOTANICAL SURVEY OF INDIA

दक्षिणीक्षेत्रीयकेन्द्र / Southern Regional Centre
टी,एन.ए.यूकैम्पस/ T.N.A.U. Campus
लाउलीरोड/ Lawley Road
कोयंबत्तूर/ Coimbatore - 641 003

टेलीफोन / Phone: 0422-2432788, 2432123, 2432487
टेलीफक्स/ Telefax: 0422- 2432835
ई-मैल/E-mail id: sc@bsi.gov.in
bsisc@rediffmail.com

सं. भा.व.स./द.क्षे.के./No.: BSI/SRC/5/23/2022/Tech /496 दिनांक/Date: 22nd September 2022

पादप प्रमाणीकरण प्रमाणपत्र / PLANT AUTHENTICATION CERTIFICATE

The plant specimen brought by you for authentication is identified as ***Spathodea campanulata*** **P.Beauv. - BIGNONIACEAE.**

अभिनिर्धारित प्रतिरूप को संबंधित कॉलेज/विभाग/संस्थान के पादपालय में परिरक्षण हेतु वापस किया जाता है।/ The identified specimen is returned herewith for preservation in their College/ Department/ Institution Herbarium.

22/9/2022

डॉ. एम. यु. शरीफ़/DR. M. U. SHARIEF
वैज्ञानिक 'एफ' एवं कार्यालयाध्यक्ष/
SCIENTIST 'F' & HEAD OF OFFICE

सेवा में / To

Ms. S. THARANI
Ph.D. Research Scholar
Department of Chemistry
Avinashilingam Institute for Home Science &
Higher Education for Women
COIMBATORE – 641 043

Avinashilingam Institute for HomeScience and Higher Education for Women
(Deemed to be University Estd. u/s 3 of UGC Act 1956, Category 'A' by MHRD
Re-accredited with A++ Grade by NAAC. CGPA 3.65/4, Category I by UGC
Coimbatore - 641 043, Tamil Nadu, India

Appendix L2

(Item No 5 of Check List) Details of Research Publications

S.No	Article	Journal	Other Details Vol/No/Page No/ Year	Published in UGC-CARE / Scopus Indexed/ Web of Science
1	Sustainable biomass conversion into activated carbon for supercapacitor devices: a promising approach toward renewable energy storage.	Energy Sources, Part A: Recovery, Utilization, and Environmental Effects	Vol.46, No.1, 1165-1176 2024	Scopus/ WoS
2	Substainable synthesis of Porous Biomass-Derived carbon from Tecoma capensis for High Performance Supercapacitors: Characterisation and Electrochemical Evaluation	Asian Journal of Chemistry	Vol.36, No.3, 710-716, 2024	Scopus indexed

*Proof of list of Journals from Internet to be attached along with copies of reprints.

Scholar : S.Tharani.

Supervisor :

Checked By: 11.3.2024

HoD/Dean of Respective School

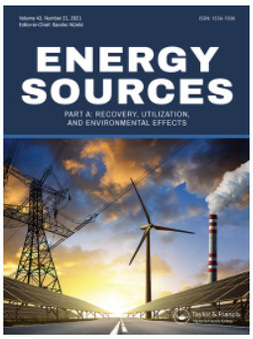

Energy Sources, Part A: Recovery, Utilization, and Environmental Effects

ISSN: (Print) (Online) Journal homepage: www.tandfonline.com/journals/ueso20

Sustainable biomass conversion into activated carbon for supercapacitor devices: a promising approach toward renewable energy storage

Tharani S & Prithiba A

To cite this article: Tharani S & Prithiba A (2024) Sustainable biomass conversion into activated carbon for supercapacitor devices: a promising approach toward renewable energy storage, Energy Sources, Part A: Recovery, Utilization, and Environmental Effects, 46:1, 1165-1176, DOI: 10.1080/15567036.2023.2293242

To link to this article: https://doi.org/10.1080/15567036.2023.2293242

ENERGY SOURCES, PART A: RECOVERY, UTILIZATION, AND ENVIRONMENTAL EFFECTS
2024, VOL. 46, NO. 1, 1165–1176
https://doi.org/10.1080/15567036.2023.2293242

Sustainable biomass conversion into activated carbon for supercapacitor devices: a promising approach toward renewable energy storage

Tharani S and Prithiba A

Department of Chemistry, Avinashilingam Institute for Home Science and Higher Education for Women, Coimbatore, India

ABSTRACT

In recent years, exploitation of biomass as an economical and environmentally friendly source for the production of energy to power supercapacitor devices has gained momentum. It is a viable alternative to current methods of energy consumption and chemical production, offering a more cost-effective and sustainable solution. Additionally, biomass has an inherently high energy capacity, making it a promising source of energy for the production of supercapacitor devices. The current investigation utilizes Spathodea campanulata leaves and flowers to synthesize KOH-activated carbon (AC) through microwave approach. In this study, two types of biomass-derived materials, AC-SPL and AC-SPF, were evaluated for their suitability as electrode materials for supercapacitors. FTIR results suggested the presence of O- and *N*- functionalities in the synthesized carbon materials. XRD results reflected an amorphous structure with an increased crystalline size due to KOH activation. The specific capacitance values of AC-SPF were found to be 9.2F/g while for AC-SPL 6.03 F/g. The investigated samples were found to possess good physicochemical properties and promising electrochemical performance, making them suitable for use in the development of an inexpensive and eco-friendly electrode material for supercapacitor applications.

ARTICLE HISTORY
Received 31 May 2023
Revised 1 December 2023
Accepted 6 December 2023

KEYWORDS
Electrode material; *Spathodea campanulata*; biomass carbon; microwave treatment; supercapacitors

Introduction

Biomass-derived carbon is identified as a promising material for supercapacitor applications due to its low cost, abundant availability, and eco-friendly nature. Supercapacitors are energy storage devices that can store and release electrical energy rapidly, making them ideal for use in applications that require high power and quick energy delivery. Traditional supercapacitor electrodes are typically made of activated carbon derived from fossil fuels, which is expensive and has a significant carbon footprint. Biomass-derived carbon, on the other hand, is obtained from renewable sources such as agricultural waste, forestry residues, and municipal solid waste. This makes it an attractive alternative to traditional activated carbon for supercapacitor electrodes. Moreover, biomass-derived carbon has several unique characteristics that make it an ideal material for supercapacitor applications. For example, it has a high surface area, which allows for a large amount of charge to be stored, and it has a high electrical conductivity, which facilitates rapid charge and discharge. Additionally, the porosity of biomass-derived carbon can be easily tailored to optimize its performance for specific applications (Guerriero et al. 2016; Yang et al. 2018). Spathodea campanulata, commonly known as the African Tulip Tree or Flame-of-the-Forest and regarded as weed, acts as potential biomass waste that can be utilized for electrode material synthesis. They contain various phytoconstituents such as alkaloids, flavonoids,

CONTACT Tharani S tharaniphd@gmail.com Department of Chemistry, Avinashilingam Institute for Home Science and Higher Education for Women, Coimbatore, India

phenols, etc., and contain significant amounts of cellulose, hemicellulose, and lignin, which are organic compounds rich in carbon. These components make the leaves suitable for conversion into carbon-based electrode materials. Similarly, the flowers consist of petals and sepals that contain organic compounds suitable for energy storage applications. By effectively harnessing the organic matter from both the leaves and flowers, it is possible to convert this biomass waste into valuable electrode materials (Yang and Park 2018). Various biomass precursors, such as Marabu wood (Farm 2020), empty oil palm fruit (Awitdrus et al. 2015), *Camellia oleifera* residue (Bo et al. 2019), waste cumin plant (Inal et al. 2018) had been studied for preparing porous carbon materials. Researchers have recently explored the use of Spathodea campanulata as a novel raw material for producing porous electrode materials. Microwave heating offers numerous advantages compared to conventional methods, with one of its most significant benefits being a substantial reduction in treatment time, leading to a consequent decrease in energy consumption. In recent years, an increasing number of researchers have turned to microwave heating for synthesizing activated carbon, resulting in a growing body of literature that examines the impact of various operational parameters on the yield and adsorption capacity of activated carbon. Chemical activation requires an impregnation ratio, whereas physical activation requires an agent flow rate, as well as radiation power and duration (Hesas et al. 2013; Huang et al. 2011).

Furthermore, activated carbons produced through microwave-assisted methods exhibit distinct characteristics compared to those prepared using conventional approaches. Apart from their larger surface area, microwave-assisted activated carbon also exhibits unique properties due to their heating mechanism differences. These microwave-derived activated carbons possess remarkable adsorption properties, which cannot be solely attributed to surface area and pore size distribution. Instead, their chemical structure plays a vital role. Microwave heating resulted in an increased adsorption capacity by virtue of carboxylic groups and higher charge density on the adsorbent surface (Franca et al. 2010; Abioye and Ani 2015).

These modified carbon materials hold potential as electrode materials in energy storage devices like supercapacitors and batteries. The aim of this research article is to delve deeper into the potential of biomass-derived carbon for supercapacitor applications and its implications for sustainable development (Nunes, Godina, and Matias 2019).

Experimental method

Preparation

The leaves and flowers of *Spathodea campanulata* were collected and then rinsed with distilled water before being dried for 12 h at 80°C. Afterward, the dried samples were crushed and placed in a muffle furnace to be pre-carbonized at 300°C for 2 h, producing the as-prepared char. To create the KOH/char composite, the char was soaked in a 6.0 M KOH solution in a 1:3 ratio for 3 h. Afterward, the sample was placed in a ceramic crucible which was then exposed to microwave radiation for 3 min at 600 W. To neutralize the pH, the sample was washed multiple times with 1.0 M HCl solution and deionized water. We designated the resulting activated carbon samples AC-SPL for leaves and AC-SPF for flowers (Liang et al. 2018). This process involved several steps. Initially, *Spathodea campanulata* undergoes pre-carbonization at a temperature of 300°C. This step involves heating the material to initiate the carbonization process and remove volatile components. After pre-carbonization, the partially carbonized material was impregnated with KOH, which acted as an activating agent. The KOH loading step ensures a uniform distribution of KOH throughout the carbon matrix. Subsequently, the KOH-loaded material was subjected to a microwave treatment. Unlike traditional high-temperature methods, microwave treatment uses a microwave field to generate heat at the molecular level (Cheng et al. 2018; Feng et al. 2018) We chose KOH as the activating agent, as the literature reveals that at lower activation temperatures, it supports a well-defined pore size distribution and generates high yields of carbon materials. The primary causes of defects and porosity in carbon

materials are H_2, CO, and CO_2 gases, which are released when KOH reacts with char-carbon at high temperatures (Tripathi, Murugavel, and Singh 2021). Because of its high carbon yield, the KOH activation method is the most efficient activation method. When porous carbon is activated with more KOH, it produces greater pores, indicating that more carbon structures were burned off during the activation process (Xu et al. 2016). Characterization studies were carried out for synthesized activated carbons to determine their structural, pore structure and morphology.

Material characterization

FT-IR spectra of as-prepared AC-SPL and AC-SPF were determined using a Perkin Elmer FT-IR spectrophotometer with the SOFTWARE – OPUS version 6.5, in the frequency range of 4000–400 cm^{-1}. UV–Visible spectra were taken using a Systronics double beam spectrometer 2202, in the wavelength range of 200–800 nm. X-Ray diffraction analysis was conducted using an X-PERT-PRO Pan analytical diffractometer, with a Cu-Kalpha (l = 1.5406 nm) X-ray source at a generator voltage of 45 KV and current of 30 mA. Raman spectra were determined using WiTec alpha 300, Germany. The surface morphology of the as-prepared activated carbon was analyzed by SEM JEOL MODEL JSM 6360.

Electrode preparation

In this study, a three-electrode system was employed to investigate the electrochemical properties of a carbon material that was synthesized using a mixture of 85% AC-SPL and AC-SPF, 10% Ketjen Black, and 5% polyvinylidene difluoride dissolved in N-methyl-2-pyrrolidinone (NMP). The prepared slurry was then coated onto a Toray carbon sheet of 1 cm^2 area and vacuum-dried at 80°C overnight. The electrochemical experiments were carried out in 1 M H_2SO_4 solution using a saturated calomel electrode as a reference electrode and a platinum wire as counter electrode.

To evaluate the electrochemical properties of the material, cyclic voltammetry (CV) was performed, and the working electrode was stabilized by cyclic voltammetry at a scan rate of 10 mV/s before conducting the measurements at different scan rates (Chaitra et al. 2016).

Results and discussions

UV–Visible spectroscopy

Ultraviolet absorption peak that is often observed in carbon-based materials has been attributed to the electronic transitions occurring between the bonding and antibonding π orbitals, specifically π-π* transitions, which are typically observable within the 180–260 nm range (Sathish-Kumar et al. 2012). Remarkably, Figure 1 highlights the distinctive absorption peak in AC-SPL and AC-SPF materials at precisely 260 nm, as a result of the electronic transitions that transpire between the bonding and antibonding π orbitals, specifically the π-π* transition (Gupta et al. 2021). However, in the case of AC-SPL and AC-SPF, the maximum absorption was detected at the 280 nm wavelength, which is indicative of an enhanced π-π* transition. Furthermore, the characteristic absorption peaks observed at 270 and 250 nm could potentially be attributed to the amplified π-π* transition that transpires in carbon-based materials.

Band-gap calculation

Absorbance of AC-SPL and AC-SPF at 254 nm is attributed to the presence of aromatic compounds, while the absorbance at 250 nm is associated with the presence of conjugated double bonds (Zhang, Wang, and Li 2014). The band gap values, which were calculated from the absorbance data, indicate the minimal amount of energy necessary to excite an electron in a material from its valence band to its

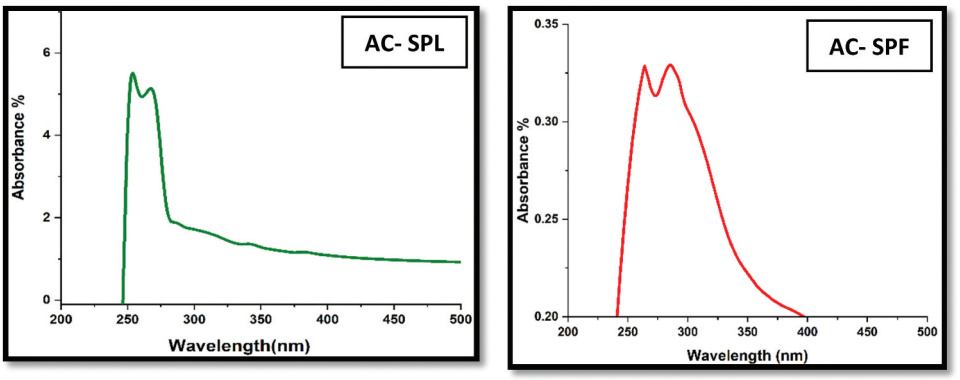

Figure 1. UV spectrum of AC-SPL and AC-SPF.

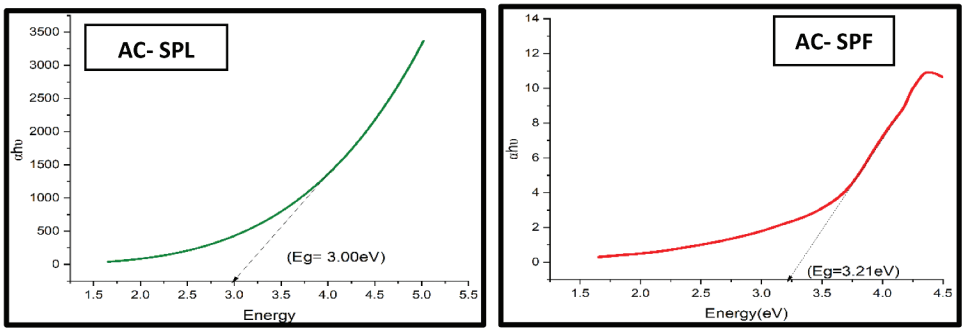

Figure 2. Tauc plot for AC-SPL and AC-SPF.

conduction band. The higher the band gap value, the more difficult it is for the electrons to be excited, resulting in lower energy storage capabilities. The energy gap for carbon materials was calculated using the formula (Gao et al. 2019; Wang et al. 2018) (Table 1),

$$E = hc/\lambda \tag{1}$$

where h = 6.626 × 10^{-34} Joules sec (Planck's constant), c = 2.99 × 108 m/s (Velocity of light), λ is the wavelength (Absorption peak value).

In this study (Figure 2), the prepared activated carbon materials were found to have band gap values of 3.00 and 3.21, respectively. These values suggest that the materials have moderate-to-high energy storage capabilities, making them potentially useful for energy storage applications such as supercapacitors.

FT-IR analysis

Surface chemical properties of synthesized activated carbon materials had been analyzed using Fourier-transform infrared spectroscopy. The evolution of chemical composition of the AC-SPL and AC-SPF was characterized by FT-IR analysis (Table 2). From the FTIR results shown in Figure 3, the peak observed at 1105 cm^{-1} may be due to the presence of C-H stretching vibration. The existence of N-containing bonds was confirmed by a peak around 1581 cm^{-1}. Additionally, a peak around 3801 cm^{-1} is assigned to the OH stretching vibration of polyphenols or hydroxyl groups, whereas in the AC-SPF, a peak at 1159 cm^{-1} indicated the presence of O-H bending vibration of alcohols. Further, the peaks at 1593 and 3805 cm^{-1} may be due to the presence of C-H stretching and

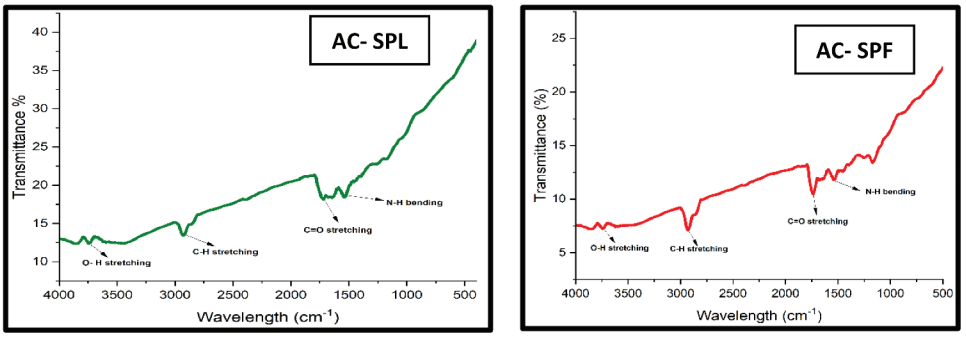

Figure 3. FTIR of AC-SPL and AC-SPF.

OH stretching vibrations, probably due to the presence of the largest percentage of phenolic OH or alkyl hydroxyl group, and an additional small shoulder peak is attained at 1745 cm^{-1} which represents the presence of C=O stretching of ester, which is electrochemically more active (Mary, Nandhini, and Bose 2019).

Raman spectroscopy analysis

A Raman spectroscopic study of biomass-derived carbon materials was conducted, and it involves the analysis of two characteristic Raman peaks and D and G-band. The D-band is related with imperfections of the carbon material, while the G-band arises due to the stretching of sp^2 carbon atoms. The D to G-band integrated intensity ratio (I_D/I_G) is a measure of the structural ordering and graphitization of carbon materials. It can be used to reveal the degree of crystallinity of a sample (Chung et al. 2020). The lower values of I_D/I_G ratio indicated a higher graphitization degree. "In-plane crystallite size La, can be determined using the Tuinstra-Koenig relationship,

$$La(nm) = (2.4x10 - 10)\lambda 4(I_D/I_G)^{-1} \quad (2)$$

Where λ = 532 nm which is the Raman excitation wavelength." The values of La are corresponding to the inter-defect distance on the surface of the carbon materials (Table 3) (Giannazzo et al. 2020).

Raman spectra of the AC-SPL and AC-SPF are shown in Figure 4; two distinctive Raman peaks were noticed intensely at about 1348 cm^{-1} and 1582 cm^{-1} for AC-SPL. The D to G-band integrated ratio (I_D/I_G) was 0.94, whereas in AC-SPF, two distinctive Raman peaks at 1370 cm^{-1} and 1587 cm^{-1} with the I_D/I_G ratio of 0.89. It has been seen that, after KOH activation, the I_D/I_G value was reduced from 0.94 to 0.89, which indicated defective sites were reoriented and hybridized carbon structures

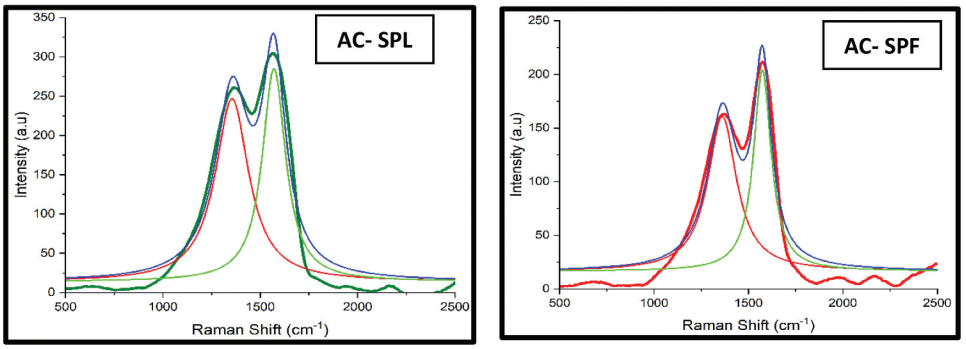

Figure 4. Raman spectra of AC-SPL and AC-SPF.

were enhanced during activation (Karaman et al. 2021). In this study, the obtained R^2 values of 0.84 and 0.81 indicate that the Lorentz fit provides a reasonably strong fit to the SPL and SPF data derived from the Raman spectra.

XRD analysis

XRD gives information about degree of structural order, average size, and interlayer distance of the carbon materials (Panicker and Sahu 2021). To analyze the graphitization of as-synthesized activated carbon materials, the XRD technique was adopted. From Figure 5, it may be noticed that XRD is amorphous in nature, and the size of particles can be calculated from the XRD data using the,

$$\text{Scherrer formula} : \text{DP} = (0.04\text{xl})/(\beta \text{x} \cos\theta) \tag{3}$$

where DP is the average crystallite size, β is the line broadening in radians, θ is the Bragg's angle, and l is the X-ray wavelength" (Katagiri, Adachi, and Ota 2014). From the XRD pattern of AC-SPF, two broad humps at about 24° and 38° are visible, which are attributed to the graphene-like domains, whereas for AC-SPL indicated at 2θ = 44° and 77°. A peak at 44° which can be attributed to the (002) diffraction peak of the amorphous nature of the carbon with low graphitization degree (Shan et al. 2016). Furthermore, an intense peak at 2Θ = 77.8° with d spacing of 1.2 Å with crystallite size of 14.38 nm corresponds to the (110) plane was observed. It was found that after KOH activation, there was enhanced crystalline size, and it will enhance the conductivity of activated carbon material (Rajasekaran and Raghavan 2020). From Table 4, the crystalline sizes of AC-SPF and AC-SPL were found to be 3.25 and 17.06 nm.

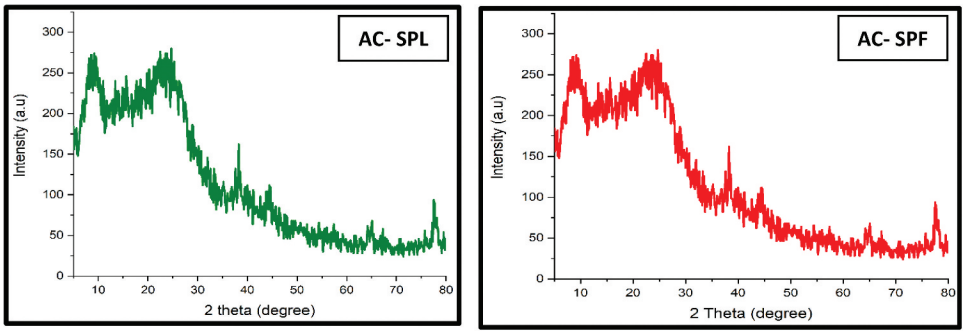

Figure 5. XRD spectra of AC-SPL and AC-SPF.

Table 1. Energy gap of carbon materials.

Carbon materials	Absorbance wavelength (nm)	Band gap of AC (eV)
AC-SPL AC	254	3.00
AC-SPF AC	250	3.21

Table 2. FT-IR analysis of AC-SPL and AC-SPF.

AC-SPL		AC-SPF	
Wavelength (cm^{-1})	Assignment	Wavelength (cm^{-1})	Assignment
1105	C-O stretch	1159	O-H bend
1581	N-H stretch	1593	N-H bend
2935	C-H stretch	1745	C=O stretch
3801	-OH stretch	2935	C-H stretch
-	-	3805	-OH stretch

Table 3. Parameters determined using Raman spectroscopy.

Materials	G band	D band	Nature	Crystalline size (La) nm
AC-SPL	1348	1582	High degree of graphitization	17.8
AC-SPF	1370	1587		18.8

Table 4. Crystalline size of AC-SPL and AC-SPF.

Carbon materials	Position (2θ)	FWHM (2θ)	d-Spacing (Å)	Crystallite size (nm)
AC-SPF	38.25	2.7	2.35113	3.25
AC-SPL	77.76	0.62530	1.22719	17.06

Thermogravimetric analysis

The rate and amount of weight change in carbon materials were determined by Thermal Gravimetric Analysis (TGA) either at a given temperature as the temperature increased or isothermally over a period. This analysis enabled researchers to observe the phase shifts due to oxidation, decomposition, or dehydration in these materials. Differential Thermal Analysis (DTA) was employed to identify whether the reaction was exothermic or endothermic.

Regarding AC-SPL and AC-SPF, TGA profiles revealed that AC-SPL's initial weight loss at 100°C was attributed to the presence of adsorbed water molecules and moisture (Nagarajan et al. 2016). A secondary weight loss of around 500°C was identified as the degradation of cellulose and hemicellulose (Oliveira 2016). For AC-SPF, the initial weight loss was observed at 100°C, and a secondary weight loss was seen around 450°C which was attributed to the decomposition of carbon (Nagarajan et al. 2016).

From Figure 6: DTA profiles inferred that the reaction is exothermic in nature with weight loss of 16.6% at around 100–400°C and a weight loss of 21.5% at around 450–800°C, whereas in AC-SPF, there was a slight endothermic reaction with absorption of small amount of energy then around 700–800°C it undergone exothermic reaction with mass loss of 15.2% at around 100–350°C and a weight loss of 25.2% at around 400–800°C.

Comparison of crystallite size in synthesized carbon materials

Crystallite size of synthesized activated carbon materials calculated from results of Raman spectroscopy and XRD techniques are tabulated in Table 5.

Scanning electron microscopy and EDAX

The morphology of the carbonized/activated material produced by the KOH-fabricated microwave-assisted method was depicted by an irregular and dense surface that exhibited a hierarchical porous structure. From Figure 7, the results of the investigation indicated that the application of microwave heating during the process of pre-carbonization was highly advantageous in terms of generating a porous structure within the material due to the rapid dipole rotation and ionic conduction which heated the pre-carbonized AC-SPF and AC-SPL. Additionally, the release of water molecules during this process supposed to generate cracks, thus increasing the porosity of the derived carbon material. Moreover, the addition of KOH further enhanced the porosity of the material (Liang et al. 2018). Elemental analysis of plant materials, AC-SPL and AC-SPF (Table 6) showed that increase in carbon and oxygen content which might be due to increase in gasification reactions. Some additional peaks were found in all the functional carbon which might belong to Cu grid used as sample holder in EDAX instrument. However, low atomic number elements are difficult to detect EDAX.

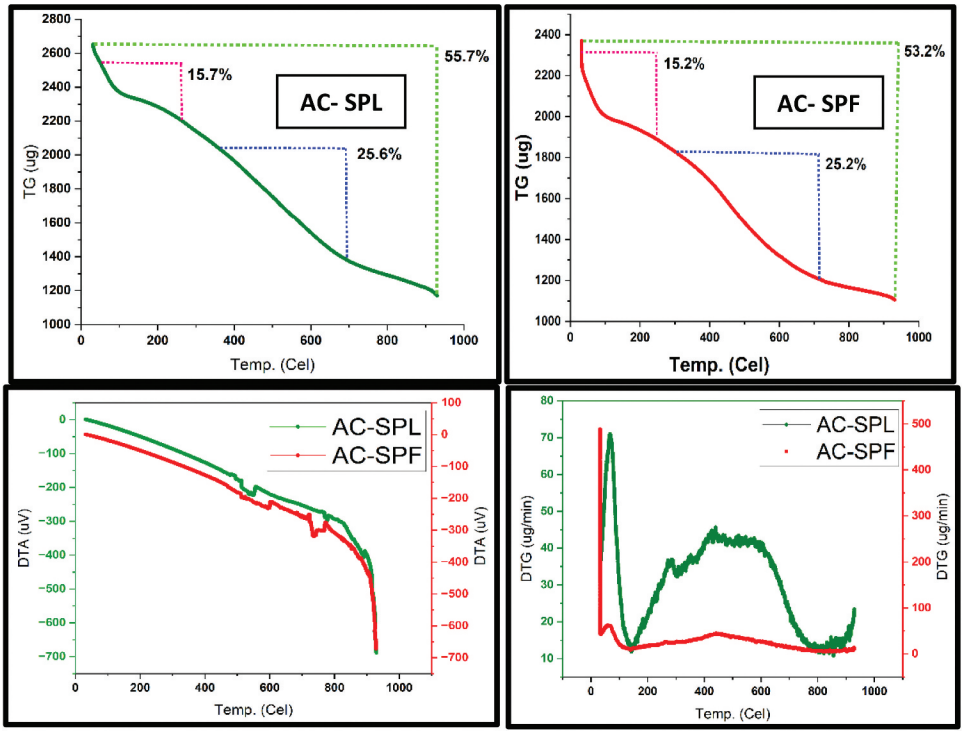

Figure 6. TGA images of AC-SPL/AC-SPF.

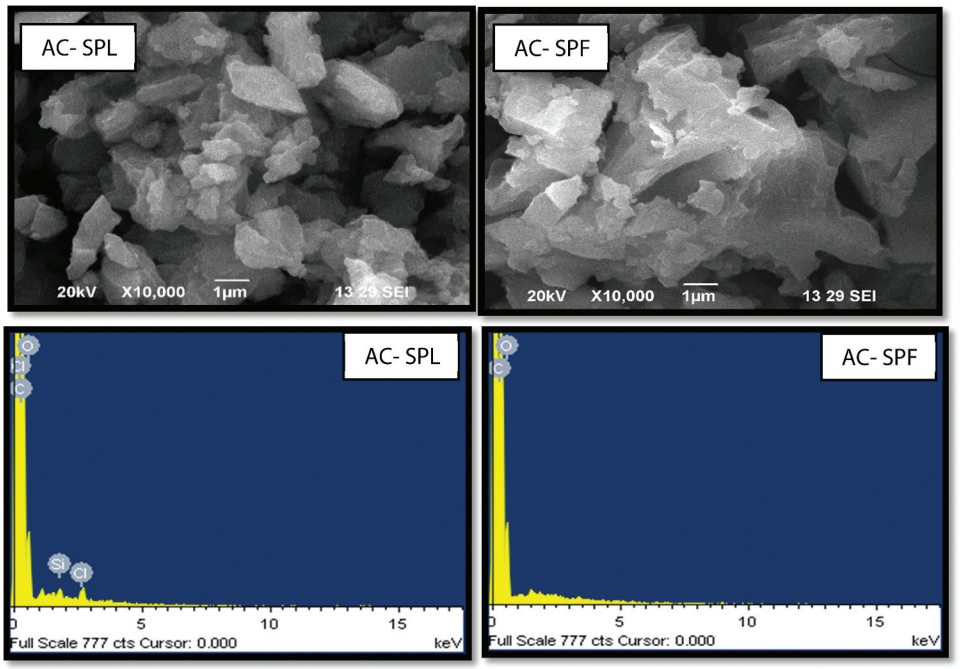

Figure 7. SEM images and elemental analysis of AC-SPL and AC-SPF.

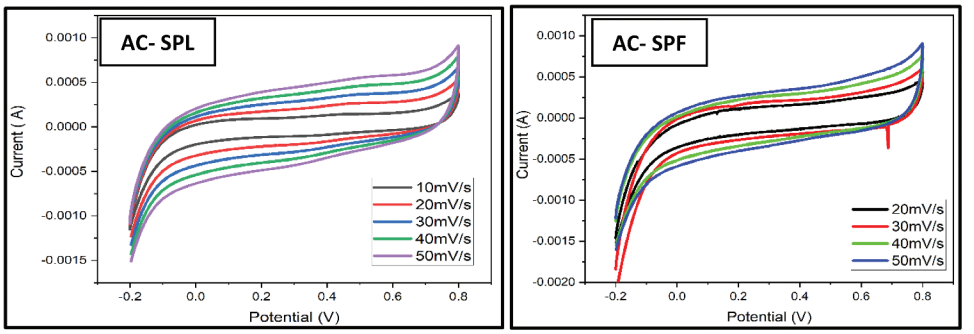

Figure 8. CV curves of AC-SPL and AC-SPF.

Table 5. Crystallite size of synthesized carbon materials.

	Crystalline size (nm)	
Carbon materials	Raman spectroscopy	XRD
AC-SPF	18.8	3.25
AC-SPL	17.8	17.06

Table 6. Elemental analysis of SPL, SPF, AC-SPL, and AC-SPF.

Element	Atomic %	Element	Atomic %	Element	Atomic %	Element	Atomic %
SPL		SPF		AC-SPL		AC-SPF	
Carbon	49.9	Carbon	51.5	Carbon	66.14	Carbon	69.31
Nitrogen	0.86	Nitrogen	2.75	Oxygen	33.24	Oxygen	30.69
Sulphur	0.13	Sulphur	0.35	Silica	0.27		
Phosphorous	0.14	Phosphorous	1.82	Chlorine	0.34		
Potassium	18.25	Potassium	15.72				
Calcium	15.5	Calcium	20.0				
Magnesium	2.30	Magnesium	3.77				
Manganese	0.011	Manganese	0.032				
Sodium	0.289	Sodium	0.181				
Aluminium	0.148	Aluminium	0.200				
Ferrous	0.060	Ferrous	0.138				

Electrochemical measurements

In order to determine the capacitive characteristics of AC-SPL and AC-SPF materials, cyclic voltammetry was used. From Figure 8, Rectangular shaped CV patterns revealed the capacitive behavior of the materials. The area under the CV curves was integrated to determine the specific capacitance (Cs) at varying scan rates, ranging from 10 to 50 mV/s, within a potential window of −0.2 to 0.8 V.

$$Cs = 1/\gamma w(Va - Vc) \tag{4}$$

Where V is the applied potential window (Va to Vc), γ is the scan rate in mV/s and w is the weight of the active material in g" (Ranga Rao et al., 2011).

Table 7 represents the obtained specific capacitance for different respective scan rates. As scan rate increased, the Cs decreased. Overall, the process was controlled by factors such as electrode resistance, output currents, and voltage drops. Our results showed that the activated carbon exhibited a specific capacitance of almost 10 Fg^{-1}, which is relatively low compared to

Table 7. Specific capacitance from cyclic voltammetry for AC-SPL/AC-SPF.

	Specific capacitance (F/g)	
Scan rate (mV/s)	SPF	SPL
10	-	9.2
20	6.03	8.4
30	5.9	7.9
40	5.4	7.5
50	5.25	7.2

Table 8. The electrochemical performance of the AC-SPL/AC-SPF samples compared to other sources.

Source	Electrolyte	Capacitance (F/g)	Electrochemical measurements	References
Petroleum pitch	6 M KOH	20	GCD	Wang et al. (2018)
Carbon nanotubes	6 M KOH	29	CV	Aria and Gharib (2012)
Graphene based supercapacitors	Ionic liquids	20	CV	Bondavalli et al. (2018)
Fluid coke derived activated carbon	Aqueous KOH	10–20	CV	Hu (2008)
Marabu wood	1 M $TEABF_4$	20	GCD	Farm (2020)
Oil palm empty fruit		23.024		
ACM10s		17.556		
ACM30s	1 M H_2SO_4	8.472	CV	Awitdrus et al. (2015)
ACM50s		1.866		
ACM70s		2.780		
Camellia oleifera residue	2 M H_2SO_4	367	CV	Bo et al. (2019)
(waste) cumin plant		117		
HCl washed cumin plant	1 M H_2SO_4	127	GCD	Inal et al. (2018)
HF washed cumin plant		155		

other studies that have reported specific capacitances ranging from 50 to 200 Fg^{-1} for activated carbon (Chen 2019; Li 2018). This result could be due to the differences in the preparation method and activation process of the activated carbon used in our study compared to other studies. However, it is important to note that a specific capacitance of 10 Fg^{-1} is still relatively high compared to other materials, such as metal oxides and conductive polymers, which typically have specific capacitances in the range of 1–10 Fg^{-1} (Wang et al. 2018).

Conclusion

In the present study, a novel approach was employed to synthesize an innovative type of porous carbon material utilizing biomass waste derived from AC-SPL/AC-SPF via a microwave-assisted carbonization/activation methodology. To comprehensively characterize the structure, surface components, and chemical states of the materials, an extensive set of analytical techniques was utilized, including FTIR, SEM, TGA, XRD, and Raman spectroscopy. The outcomes of the investigations revealed that the material exhibited noteworthy electrochemical activity and was oxygen-functionalized, highlighting its immense potential for multifarious applications. Therefore, activated carbon still holds promise as an electrode material for energy storage applications, and further optimization of the preparation and activation process could potentially improve its specific capacitance.

Disclosure statement

No potential conflict of interest was reported by the author(s).

Funding

This work was supported by the Department of Science and Technology, Ministry of Science and Technology, India; DST-CURIE-AI Facility.

ORCID

Tharani S http://orcid.org/0000-0002-6919-6668

References

Abioye, A. M., and F. N. Ani. 2015. Recent development in the production of activated carbon electrodes from agricultural waste biomass for supercapacitors: A review. *Renewable and Sustainable Energy Reviews* 52:1282–1293.

Aria, A. I., and M. Gharib. 2012. Effect of dry oxidation on the performance of carbon nanotube arrays electrochemical capacitors. *MRS Online Proceedings Library (OPL)* 1407:mrsf11–1407. doi:10.1557/opl.2012.543.

Awitdrus, A., M. Deraman, I. A. Talib, R. Farma, R. Omar, M. M. Ishak, and N. S. M. Nor. 2015, April. Physical and electrochemical properties of supercapacitor composite electrodes prepared from biomass carbon and carbon from green petroleum coke. *AIP Conference Proceedings* 1656(1):030007. AIP Publishing LLC.

Bondavalli, P., G. Pognon, E. Koumoulos, and C. Charitidis. 2018. Dynamic air-brush deposition method for the New generation of graphene based supercapacitors. *MRS Advances* 3 (1–2):79–84. doi:10.1557/adv.2018.65.

Bo, X., K. Xiang, Y. Zhang, Y. Shen, S. Chen, Y. Wang, M. Xie, and X. Guo. 2019. Microwave-assisted conversion of biomass wastes to pseudocapacitive mesoporous carbon for high-performance supercapacitor. *Journal of Energy Chemistry* 39:1–7. doi:10.1016/j.jechem.2019.01.006.

Chaitra, K., P. Sivaraman, R. T. Vinny, U. M. Bhatta, N. Nagaraju, and N. Kathyayini. 2016. High energy density performance of hydrothermally produced hydrous ruthenium oxide/multiwalled carbon nanotubes composite: Design of an asymmetric supercapacitor with excellent cycle life. *Journal of Energy Chemistry* 25 (4):627–35. doi:10.1016/j.jechem.2016.04.012.

Chen, C. 2019. Activated carbon from sludge by one-step ZnCl2 activation for high-performance supercapacitors. *Electrochimica Acta* 293:256–264.

Cheng, Y., B. Li, Y. Huang, Y. Wang, J. Chen, D. Wei, and Y. Zhou. 2018. Molten salt synthesis of nitrogen and oxygen enriched hierarchically porous carbons derived from biomass via rapid microwave carbonization for high voltage supercapacitors. *Applied Surface Science* 439:712–723. doi:10.1016/j.apsusc.2018.01.006.

Chung, H.-Y., G.-T. Pan, Z.-Y. Hong, C.-T. Hsu, S. Chong, T. C.-K. Yang, and C.-M. Huang. 2020. Biomass-derived porous carbons derived from soybean residues for high-performance solid-state supercapacitors. *Molecules* 25 (18):4050. doi:10.3390/molecules25184050.

Farm, Y. Y. (2020). Biomass derived activated carbon as electrode materials for electrochemical double layer capacitors (EDLC). Doctoral dissertation, University of Sheffield.

Feng, Z., K. Odelius, G. K. Rajarao, and M. Hakkarainen. 2018. Microwave carbonized cellulose for trace pharmaceutical adsorption. *Chemistry Engineering Journal* 346:557–66. doi:10.1016/j.cej.2018.04.014.

Franca, A. S., L. S. Oliveira, A. A. Nunes, and C. C. Alves. 2010. Microwave assisted thermal treatment of defective coffee beans press cake for the production of adsorbents. *Bioresource Technology* 101 (3):1068–1074. doi:10.1016/j.biortech.2009.08.102.

Gao, Y., X. Yan, H. Zhang, X. Ding, and M. Liu. 2019. Activated carbon derived from walnut shell as electrode material for supercapacitors with enhanced electrochemical performance. *Journal of Alloys and Compounds* 778:185–192.

Giannazzo, F., R. Dagher, E. Schilirò, S. E. Panasci, G. Greco, G. Nicotra, and A. Michon. 2020. Nanoscale structural and electrical properties of graphene grown on AlGaN by catalyst-free chemical vapor deposition. *Nanotechnology* 32 (1):015705. doi:10.1088/1361-6528/abb72b.

Guerriero, G., J. Hausman, J. Strauss, H. Ertan, and K. S. Siddiqui. 2016. Lignocellulosic biomass: biosynthesis, degradation, and industrial utilization. *Engineering in Life Sciences* 16 (1):1–16. doi:10.1002/elsc.201400196.

Gupta, G. K., P. Sagar, S. K. Pandey, M. Srivastava, A. K. Singh, J. Singh, A. Srivastava, S. K. Srivastava, and A. Srivastava. 2021. In situ fabrication of activated carbon from a bio-waste Desmostachya bipinnata for the improved supercapacitor performance. *Nanoscale Research Letters* 16 (1):1–12. doi:10.1186/s11671-021-03545-8.

Hesas, R. H., W. M. A. W. Daud, J. N. Sahu, and A. Arami-Niya. 2013. The effects of a microwave heating method on the production of activated carbon from agricultural waste: A review. *Journal of Analytical and Applied Pyrolysis* 100:1–11. doi:10.1016/j.jaap.2012.12.019.

Hu, C. 2008. Fluid coke derived activated carbon as electrode material for electrochemical double layer capacitor.

Huang, L., Y. Sun, W. Wang, Q. Yue, and T. Yang. 2011. Comparative study on characterization of activated carbons prepared by microwave and conventional heating methods and application in removal of oxytetracycline (OTC). *Chemistry Engineering Journal* 171 (3):1446–53. doi:10.1016/j.cej.2011.05.041.

Inal, I. I. G., S. M. Holmes, E. Yagmur, N. Ermumcu, A. Banford, and Z. Aktas. 2018. The supercapacitor performance of hierarchical porous activated carbon electrodes synthesised from demineralised (waste) cumin plant by microwave pretreatment. *Journal of Industrial and Engineering Chemistry* 61:124–32. doi:10.1016/j.jiec.2017.12.009.

Karaman, C., O. Karaman, N. Atar, and M. L. Yola. 2021. Sustainable electrode material for high-energy supercapacitor: Biomass-derived graphene-like porous carbon with three-dimensional hierarchically ordered ion highways. *Physical Chemistry Chemical Physics* 23 (22):12807–12821. doi:10.1039/D1CP01726H.

Katagiri, N., N. Adachi, and T. Ota. 2014. Preparation and evaluation of ferrite-silica aerogel nanocomposite. *Journal of the Ceramic Society of Japan* 122 (1421):29–34. doi:10.2109/jcersj2.122.29.

Li, H. 2018. High-performance porous carbons from biomass wastes for supercapacitors. *Journal of Power Sources* 378:542–550.

Liang, J., T. Qu, X. Kun, Y. Zhang, S. Chen, Y. C. Cao, and M. Xie, X. Guo. 2018. Microwave assisted synthesis of Camellia oleifera shell-derived porous carbon with rich oxygen functionalities and superior supercapacitor performance. *Applied Surface Science* 436:934–40. doi:10.1016/j.apsusc.2017.12.142.

Mary, A. J. C., C. Nandhini, and A. C. Bose. 2019. Hierarchical porous structured N-doped activated carbon derived from Helianthus annuus seed as a cathode material for hybrid supercapacitor device. *Materials Letters* 256:126617. doi:10.1016/j.matlet.2019.126617.

Nagarajan, S., K. Subramani, K. Manickavasakam, N. Iiayaraja, and M. Sathish. 2016. Biomass-derived activated porous carbon from rice straw for high energy symmetric supercapacitor in aqueous and non-aqueous electrolytes. *Energy & Fuels* 31 (1):977–985. doi:10.1021/acs.energyfuels.6b01829.

Nunes, L. J. R., R. Godina, and J. C. D. O. Matias. 2019. Technological innovation in biomass energy for the sustainable growth of textile industry. *Sustainability* 11 (2):528. doi:10.3390/su11020528.

Oliveira, G. F. D. 2016. Produção de carvão ativado a partir do pecíolo do babaçu.

Panicker, N. J., and P. P. Sahu. 2021. Green reduction of graphene oxide using phytochemicals extracted from pomelo grandis and Tamarindus indica and its supercapacitor applications. *Journal of Materials Science: Materials in Electronics* 32 (11):15265–78. doi:10.1007/s10854-021-06077-0.

Rajasekaran, S. J., and V. Raghavan. 2020. Facile synthesis of activated carbon derived from Eucalyptus globulus seed as efficient electrode material for supercapacitors. *Diamond and Related Materials* 109:108038. doi:10.1016/j.diamond.2020.108038.

Sathish-Kumar, K., G. Vazquez-Huerta, A. Rodriguez-Castellanos, H. M. Poggi-Varaldo, and O. Solorza-Feria. 2012. Microwave assisted synthesis and characterizations of decorated activated carbon. *International Journal of Electrochemical Science* 7 (6):5484–5494. doi:10.1016/S1452-3981(23)19636-2.

Shan, D., J. Yang, W. Liu, J. Yan, and Z. Fan. 2016. Biomass-derived three-dimensional honeycomb-like hierarchical structured carbon for ultrahigh energy density asymmetric supercapacitors. *Journal of Materials Chemistry A* 4 (35):13589–602. doi:10.1039/C6TA05406D.

Tripathi, A. K., S. Murugavel, and R. K. Singh. 2021. Dead ashoka (Saraca asoca) leaves–derived porous activated carbons and flexible iongel polymer electrolyte for high-energy-density electric double-layer capacitors. *Materials Today Sustainability* 11-12:100062. doi:10.1016/j.mtsust.2021.100062.

Wang, Z., J. Zhang, J. Li, X. Li, and Z. Zhang. 2018. Activated carbon derived from pomelo peel as anode material for high-performance lithium-ion batteries. *Journal of Materials Science: Materials in Electronics* 29 (17):14510–14518.

Xu, M., Q. Huang, R. Sun, and X. Wang. 2016. Simultaneously obtaining fluorescent carbon dots and porous active carbon for supercapacitors from biomass. *RSC Advances* 6 (91):88674–88682. doi:10.1039/C6RA18725K.

Yang, Z., H. Lei, K. Qian, Y. Zhang, and E. Villota. 2018. Renewable bio-phenols from in situ and ex situ catalytic pyrolysis of Douglas fir pellet over biobased activated carbons. *Sustainable Energy and Fuels* 2 (4):894–904. doi:10.1039/C7SE00607A.

Yang, G., and S.-J. Park. 2018. MnO2 and biomass-derived 3D porous carbon composites electrodes for high performance supercapacitor applications. *Journal of Alloys and Compounds* 741:360–67. doi:10.1016/j.jallcom.2018.01.108.

Zhang, X., Y. Wang, and X. Li. 2014. UV-vis spectroscopic characterization of activated carbons. *Journal of Materials Science and Engineering* 4 (2):1–6.

Asian Journal of Chemistry; Vol. 36, No. 3 (2024), 710-716

ASIAN JOURNAL OF CHEMISTRY

https://doi.org/10.14233/ajchem.2024.31041

Sustainable Synthesis of Porous Biomass-Derived Carbon from *Tecoma capensis* for High Performance Supercapacitors: Characterization and Electrochemical Evaluation

S. THARANI*, and A. PRITHIBA

Department of Chemistry, Avinashilingam Institute for Home Science and Higher Education for Women, Coimbatore-641043, India

*Corresponding author: E-mail: tharaniphd@gmail.com

Received: 10 December 2023; *Accepted*: 6 February 2024; *Published online*: 28 February 2024; AJC-21565

Biowaste carbon products possess interesting physico-chemical properties and are cost-effective due to their remarkable characteristics. Biomass carbon derived from *Tecoma capensis* (TCL) was processed using pyrolysis at a controlled temperature in an eco-friendly, innovative and sustainable way to develop biomass-derived carbon material. The aim of this study is to demonstrate the facile synthesis of porous carbon compounds from biowaste and evaluate their use in supercapacitors. Various analytical methods, such as structural analysis, morphological studies and electrochemical studies, have been employed to characterize the carbon material generated from biomass. Electrochemical performance evaluation was conducted through cyclic voltammetry and galvanostatic charge-discharge studies utilizing 1 M H_2SO_4 and 1 M KOH aqueous electrolyte, which exhibited a specific capacitance of 238 F g^{-1}. The outcomes of the studies suggested that the eco-friendly, straightforward process can be utilized to prepare biomass carbon for the electrochemical energy storage applications in an efficient and sustainable manner.

Keywords: ***Tecoma capensis,*** **Biomass, Pyrolysis, Supercapacitors.**

INTRODUCTION

The release of greenhouse gases from non-renewable conventional fossil fuels is an important factor behind the global demand to switch to renewable energy sources [1-4]. However, some of the most promising sustainable energy options, such as solar, wind and hydropower, are inherently intermittent, necessitating the development of effective energy storage solutions to ensure a stable energy supply [5-7]. Supercapacitors are promising electrochemical energy storage devices that offer distinct advantages, including enhanced safety and extended cycling stability compared to conventional batteries [8-10]. Supercapacitors operate in a dendrite-free and low heat-generation mode, significantly reducing safety concerns [11-13]. Moreover, they boast an impressive cycling life of up to 100,000 cycles, far surpassing that of advanced batteries, which typically endure fewer than 10,000 cycles [11,14]. Supercapacitors show significant potential, especially in conditions that need fast charging and long-term cycle stability. Nevertheless, the energy density of supercapacitors, currently around 5 Wh/kg, falls significantly short of that of batteries, which can reach up to 200 Wh/kg [11,13,15]. The enhancement of the energy density of supercapacitors is a pressing objective.

Carbon materials are extensively employed as electrode materials for supercapacitors and their structure and composition play pivotal roles in enhancing their performance [11]. The supercapacitor capacitance relies on the interfacial reactions occurring on the electrode materials. Carbon materials with high specific surface areas and hierarchical porous structures offer an increased number of reaction sites and superior reaction kinetics [11,16,17]. Additionally, the introduction of heteroatoms through the doping of carbon materials can fine-tune their electronic structure and induce pseudo-capacitance, further enhancing their performance [18].

Biomass-derived carbon is a versatile carbon-based material that is applied across various fields, including catalysts, adsorbents and electrodes [19-22]. Among biomass sources, coconut shells stand out due to their abundant availability, high carbon content, excellent adsorption capabilities and environmental friendliness [23-27]. The conversion of biomass into carbon materials involves carbonization or pyrolysis, where the organic precursors undergo thermal decomposition under controlled

conditions. This results in the formation of carbon materials with tailored properties which are suitable for energy storage applications. Various researchers have investigated the energy-storage properties of biomass-derived carbon materials with and without chemical activation. Sunflower shells [28], marula nutshell waste [29], lotus calyx biowaste [30], hazelnut shell waste [31] and wolfberry fruit biowaste [32] exhibit specific capacitances. *Tecoma capensis*, commonly referred to as cape honeysuckle, is characterized by its distinctive leaves, which hold potential as a biomass waste source for electrode material production. Considering these leaves for the production of electrode materials, their high cellulose content is of particular interest. Cellulose, a complex carbohydrate, can be converted into carbon-rich materials through controlled processes such as pyrolysis or carbonization. This conversion yielded a porous carbon structure with a high surface area, which is advantageous for the electrode applications.

EXPERIMENTAL

The biomass derived from *Tecoma capensis* was procured abundantly from the college campus. Initially, the biomass was subjected to thorough washing and dried in an oven, maintaining a temperature of 60 ºC. For the production of functional carbon, a precisely measured quantity of 10 g of dried leaves powder was subjected to a controlled heating process. This heating was performed in an alumina crucible at an elevated temperature of 700 ºC. Importantly, this thermal transformation occurred in an argon atmosphere, which effectively shielded the material from unwanted interactions. The heating rate was maintained at 10 ºC/min in a tubular furnace. Following a controlled heating process, a solid black residue was obtained and then washed thoroughly with 5 mol/L HCl solution. This step effectively removed any residual impurities and unwanted components from the carbonized material. The material was then dried for 12 h at 60 ºC. The resulting material, derived from the just-carbonized sample at 700 ºC, is denoted as TCL-700 [33].

Characterization: Fourier transform infrared (FT-IR) spectra of the as-prepared TCL were acquired using a Perkin Elmer FT-IR spectrophotometer, employing SOFTWARE-OPUS version 6.5. Spectral analysis covered a frequency range of 4000-400 cm^{-1}. The UV-visible spectra were recorded using a Systronics double-beam spectrometer 2202, spanning a wavelength range of 200-800 nm. X-ray diffraction (XRD) analysis was performed using an X-PERT-PRO Pan analytical diffractometer using Cu*K*α (λ = 1.5406 nm) X-ray source operated at a generator voltage of 45 KV and a current of 30 mA. Raman spectra were obtained utilizing the WiTec alpha 300 instrument, Germany. The surface morphology of activated carbon, in its as-prepared state was examined using a scanning electron microscope (SEM) with a JEOL MODEL JSM 6360 instrument.

Fabrication of electrode: For the electrochemical measurements, biomass-derived carbon (TCL-700) served as the working electrode. TCL-700 carbon, Super-P, in combination with PVDF, was employed as binder at a mass ratio of 85:10:5. The resulting mixture was homogenized to form a paste that was subsequently coated onto the graphene sheet. This three-electrode system featured 1 M KOH and 1 M H_2SO_4 as electrolytes. In this setup, the TCL carbon electrode material was employed as working electrode, Ag/AgCl (SCE) was utilized as reference electrode and platinum was used as counter electrode. Both cyclic voltammetry (CV) and galvanostatic charge-discharge (GCD) analyses were performed within a defined potential range spanning from -0.2 to 0.8 V. Various scan rates ranging from 10 to 50 mV/s were applied during the CV analysis, whereas different current densities at various ranges were considered during the GCD analysis. These electrochemical assessments collectively provide a comprehensive understanding of the electrochemical properties and performance characteristics of TCL-derived carbon materials [34].

RESULTS AND DISCUSSION

Phytochemical screening: A phytochemical screening test was used to identify the active phytochemical constituents present in the leaves extract of *T. capensis* (TCL). The analysis revealed the presence of flavonoids, alkaloids, saponins, steroids and other secondary metabolites in the ethanolic extract of TCL [35,36], which confirmed the presence of several nitrogen- and oxygen-rich compounds. These phytoconstituents in the extract may be responsible for the self-activation of samples with high porosity and conductivity.

FT-IR spectral studies: TCL exhibited distinctive peaks at 3514 cm^{-1} (O-H *str.*), 1516 cm^{-1} (C=C *str.* arom.), 1743 cm^{-1} (C=O *str.*) and 1462 cm^{-1} (C-H bend. in arom.) [37] (Fig. 1a). The FTIR spectrum of TCL-700 revealed distinctive peaks at 2361 cm^{-1} (C≡N *str.*), 1517, 1545 and 1502 cm^{-1} (arom. C=C *str.*) (Fig. 1b), indicating the presence of potentially nitrogen containing and aromatic structures. The peak at 3740 cm^{-1} (O-H *str.*) suggests the existence of hydroxyl groups, which can influence the electrochemical behaviour of the material [38]. Furthermore, the peak at 1742 cm^{-1} (C=O *str.*) indicated the presence of carbonyl groups, while the aliphatic C-H stretching vibrations appeared at 2923 cm^{-1}. The overall composition and structure of TCL-700 material play a crucial role in determining its electrochemical properties.

XRD studies: The XRD spectrum of TCL-700 (Fig. 2) exhibiting the typical peaks around 2θ = 77.5º, 43.9º and 64.5º, which indicates that the prepared TCL carbons represent graphitic carbon [33] or a crystalline nature. The analysis showed that the structure of obtained carbon material was crystalline, as indicated by the miller indices of (222), (220) and (200). Using the Debye-Scherrer's formula, the crystalline size of the carbon material was found to be 31.03 nm [39].

Raman spectral studies: The Raman spectrum of TCL-700 (Fig. 3) and shows the characteristic D and G bands at 1349 and 1583 cm^{-1}, respectively. Typically, the ratio of the intensities of these bands, known as I_D/I_G, serves as an indicator of the degree of graphitization and imperfections within the carbon materials. For TCL-700, the I_D/I_G ratio of 0.98 signifies a prominent level of graphitization, aligned well with the FT-IR spectral analysis.

To precisely determine the positions and widths of the D- and G-bands, a Lorentzian fit was employed. The statistical analysis of the Lorentzian fit yielded an R^2 value of 0.93 for

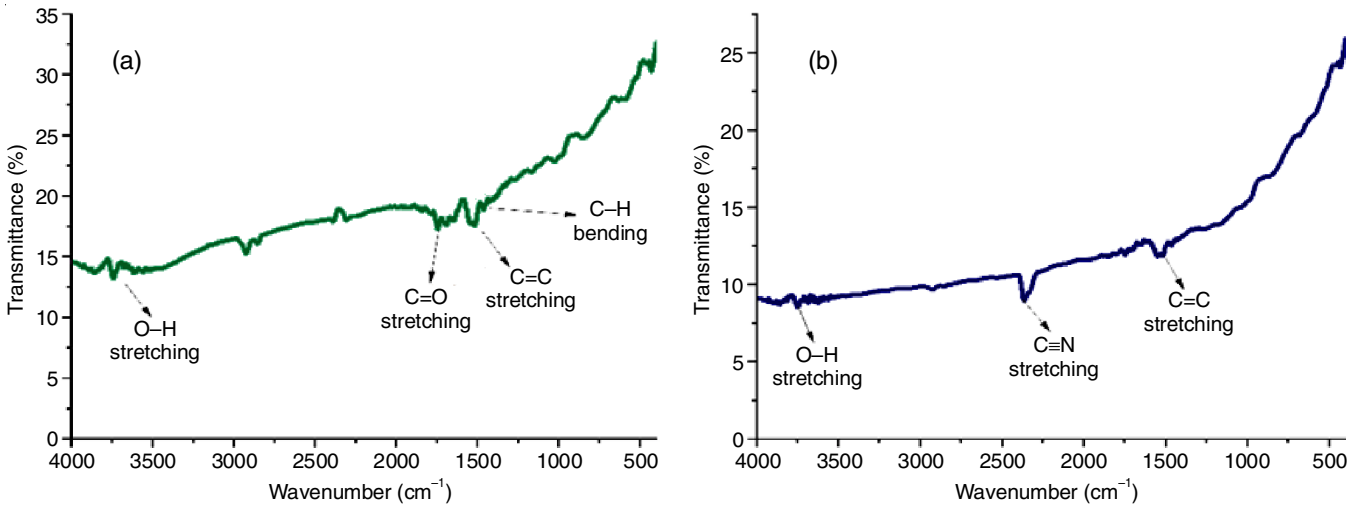

Fig. 1. FTIR spectra of *Tecoma capensis* leaves (a) and TCL-700 (b)

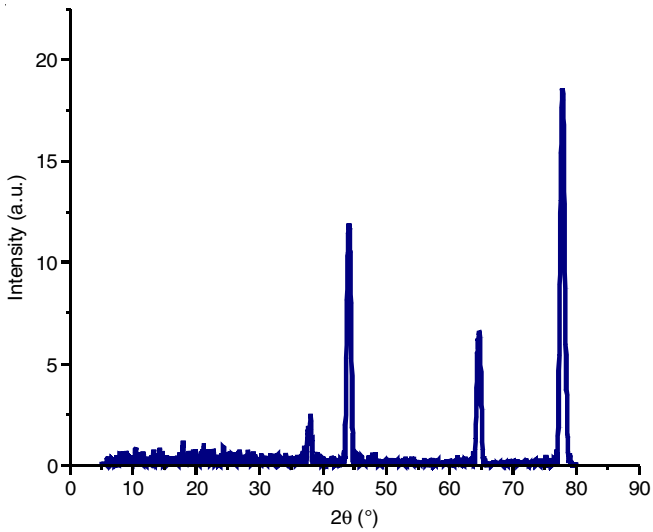

Fig. 2. XRD spectra of TCL-700

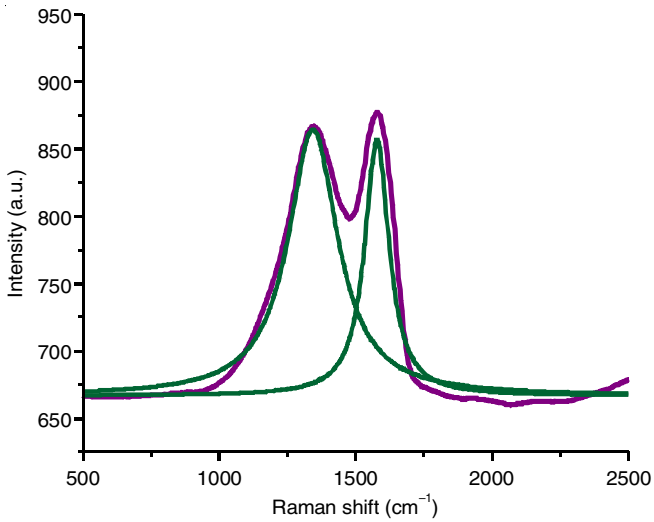

Fig. 3. Raman spectra of TCL-700

TCL-700, indicating an excellent fit of the Lorentzian model to the experimental data. This high R^2 value, near unity, suggests that the regression predictions of the Lorentzian-type model were an exceptional match for the data collected [40-42]. In-plane crystallite size (La) can be determined using the Tuinstra-Koenig relationship:

$$La\ (nm) = (2.4 \times 10^{-10})\ \lambda 4\ (I_D/I_G)^{-1}$$

where $\lambda = 532$ nm which is the Raman excitation wavelength. The values of La are corresponding to the inter defect distance on the surface of the carbon material [41]. The crystalline size of TCL-700 was found to be 17.45 nm.

FE-SEM and EDAX analysis: The FE-SEM images of the TCL produced at 700 ºC are shown in Fig. 4a-e. Additionally, a small number of pores of different sizes may be produced as byproducts of the decomposition and volatilization of raw materials. When the temperature was raised to 700 ºC, large quantities of volatile matter were released at a rapid rate, which caused the particle surface to change, shrink and split during the thermal change. An irregular surface structure was evident in the morphology of TCL-700 material. An increase in the presence of pores and the emergence of elongated channels has been observed in carbon materials [43]. Furthermore, the thermal degradation of chemical bonds and the fusion of certain compounds may result in the rupture of these bonds and alteration of the original material's structure, consequently generating larger pores [44,45].

The elemental composition of the TCL-700 sample was determined by energy-dispersive X-ray analysis (EDAX). The EDAX spectra (Fig. 4f) illustrated the elemental distribution across various regions of the sample surface, revealing the predominant presence of carbon, oxygen and nitrogen atoms in the sample [46].

Thermogravimetric studies: Thermogravimetric analysis (TGA) profiles of the TCL-700 sample are shown in Fig. 5a. These profiles exhibited different stages of weight loss occurring within two distinct temperature ranges *viz.* 85-100 ºC and 650-670 ºC. The former temperature range is attributed to the desorption of physically adsorbed water, whereas the latter corresponds to carbon pyrolysis [47]. Remarkably, even at 1000 ºC, approximately 70% of the initial sample weight remained intact.

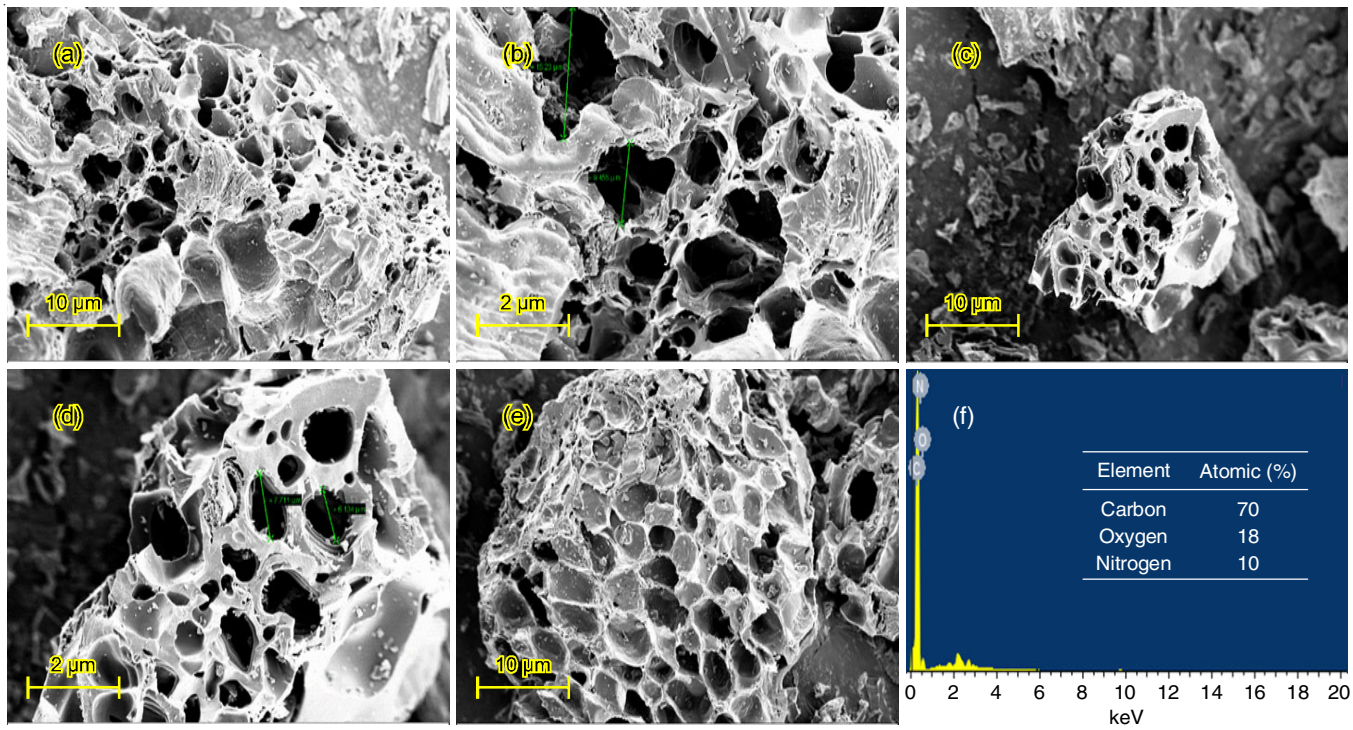

Fig. 4. FE-SEM images and EDAX spectra of TCL-700

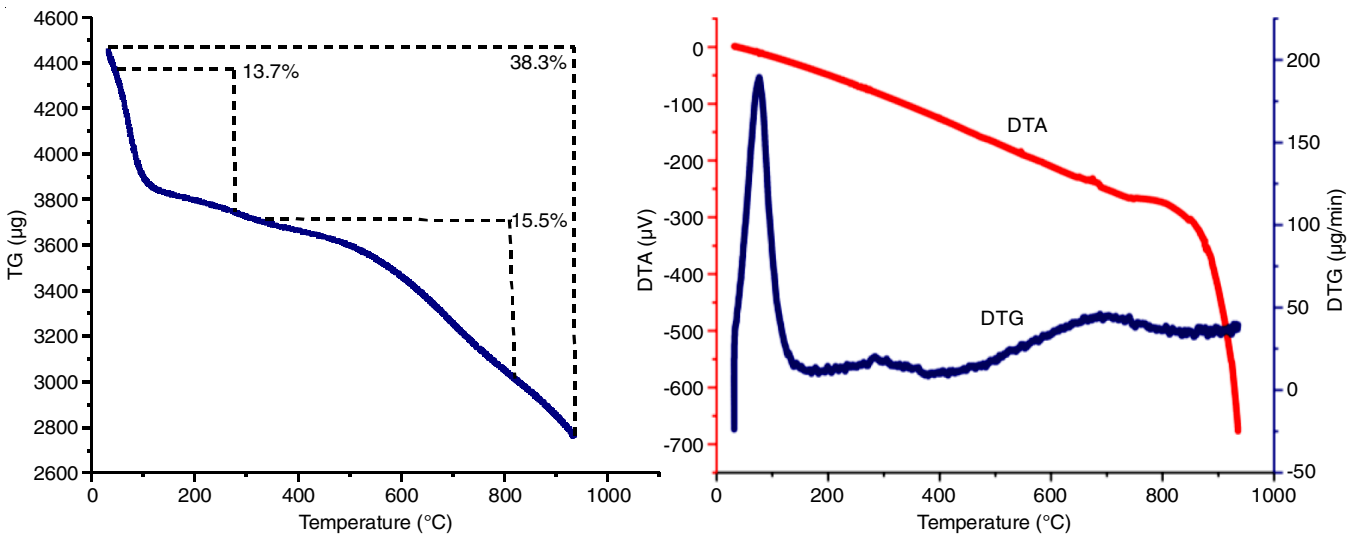

Fig. 5. TG/DTA analysis of TCL-700

Electrochemical measurements: The electrochemical assessment employed a three-electrode system, utilizing the TCL-700 coated electrode as working electrode, Pt as auxiliary electrode and Ag/AgCl as reference electrode, along with 1 M KOH and 1 M H_2SO_4 electrolytes. This setup facilitated galvanostatic charge-discharge (GCD) and cyclic voltammetry (CV) measurements to investigate electrochemical performance. The specific capacitance (Cs) of the carbon electrode material in the three-electrode system was calculated using the discharge characteristics obtained from GCD using the following formula:

$$Cs = I \times \frac{\Delta t}{(\Delta V \times m)}$$

where Cs represents the specific capacitance, I denotes the discharge current, Δt corresponds to the discharge time, m is the mass of the active material and ΔV indicates the potential window after the IR drop [48]. The cyclic voltammetry (CV) measurements of TCL-700 material, conducted using 1 M KOH and 1 M H_2SO_4 solutions as electrolytes and displayed in Fig. 6 within the voltage range of -0.2 to 0.8 V at varying scan rates (10 to 50 mV s^{-1}), provide the valuable insights. An ideal supercapacitor is often characterized by a rectangular cyclic voltammetry (CV) curve. In case of TCL-700 material, an electric double layer capacitor (EDLC) mechanism was evident when using 1 M KOH, while 1 M H_2SO_4 exhibited characteristics of pseudocapacitance. This distinction in behaviour signifies an

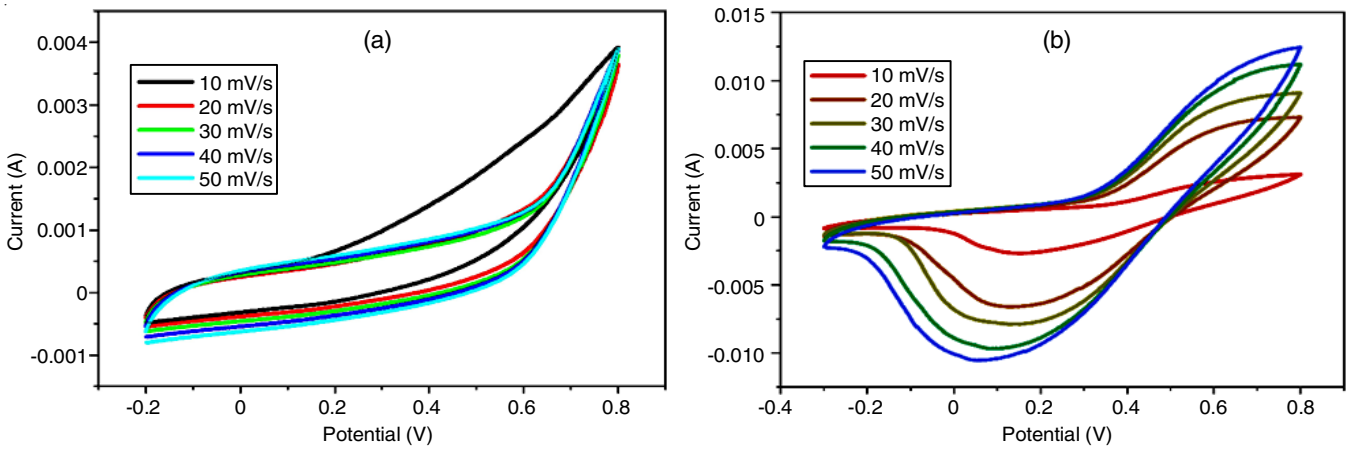

Fig. 6, Cyclic voltammetry of TCL-700 of the electrolyte (a) 1 M KOH and (b) 1 M H_2SO_4

enhancement in the electronic conductivity within the sample. Typically, materials exhibiting pseudocapacitance manifest oxidation and reduction peaks, which were observed in TCL-700, indicating the coexistence of EDLC and pseudocapacitive mechanisms. The presence of chemical bonding in the sample significantly amplified the current levels and facilitated the formation of reduction peaks. In general, the electrochemical stability of EDLC surpasses that of pseudocapacitors, contributing to TCL-700's high electrochemical performance attributed to its exceptional electrochemical properties.

In the galvanostatic charge-discharge (GCD) tests, the existence of mesopores significantly facilitates the swift movement and migration of ions during the charging/discharging phases. The GCD curves of TCL-700, illustrated in Fig. 7 across a potential range of -0.4 V to 0.4 V at various current densities ranging from 75 to 250 μA g^{-1}, revealed specific capacitance values of 238 F g^{-1} and 32.42 F g^{-1} for 1 M KOH and 1 M H_2SO_4, respectively. TCL-700 material displayed nearly triangular GCD profiles indicating the electric double-layer capacitor (EDLC) behaviour primarily with a minor pseudocapacitive effect.

Furthermore, the impedance spectra of TCL-700 presented in Fig. 8 showed the equivalent series resistance (ESR) intercepting the real axis in the high-frequency zone within electrochemical impedance spectroscopy (EIS). The ESR measurements exhibited a significant decrease in the presence of 1 M H_2SO_4 (9.8 Ω) as compared to 1 M KOH (14.8 Ω), suggesting a higher level of conductivity in the former (Table-1). Similarly, the charge transfer resistance values of 10.4 Ω and 13.8 Ω were observed for 1 M KOH and 1 M H_2SO_4, respectively. The elevated charge transfer resistance in 1 M H_2SO_4 is attributed to the combination of poor electrode conductivity and electrolyte characteristics. These findings provide insight into the electrochemical characteristics of TCL-700 material, confirming its capacity for efficient energy storage and utilization [49].

Conclusion

In conclusion, the utilization of *Tecoma capensis* (TCL) biowaste through controlled-temperature pyrolysis has proven to be a promising and eco-friendly approach to produce biomass derived carbon with the exceptional properties. Comprehensive characterization involving the structural, morphological and electrochemical analyses revealed the potential of this carbon material for the supercapacitor applications. The synthesized biomass carbon material exhibited a specific capacitance of 230 F g^{-1} in both 1 M H_2SO_4 and 1 M KOH electrolytes indicating its viability for energy storage. These findings not only emph-

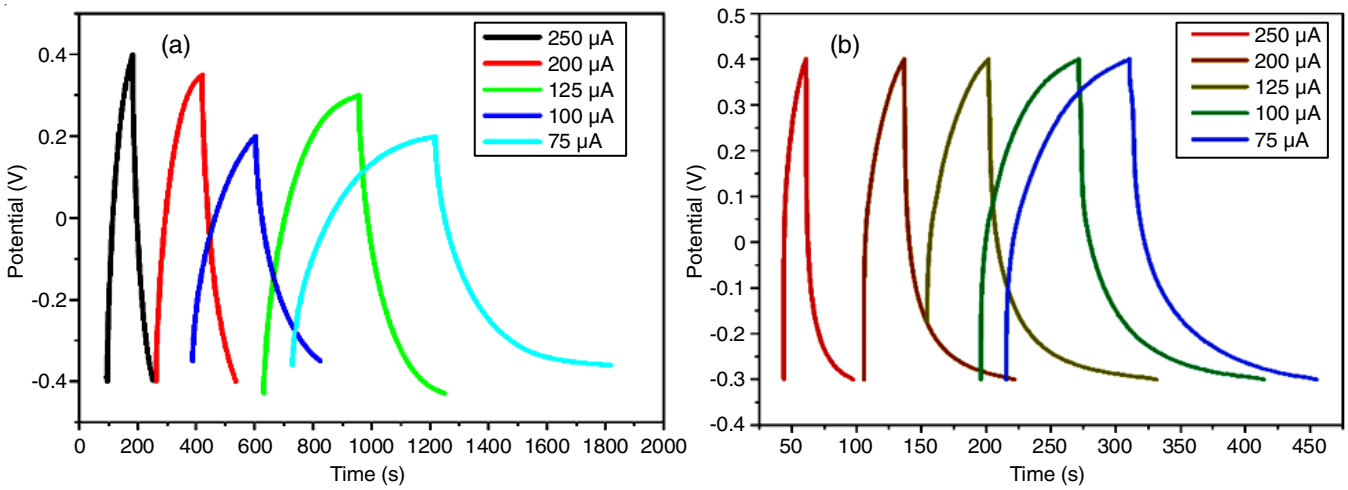

Fig. 7. GCD measurements of TCL-700 of the electrolyte (a) 1 M KOH and (b) 1 M H_2SO_4

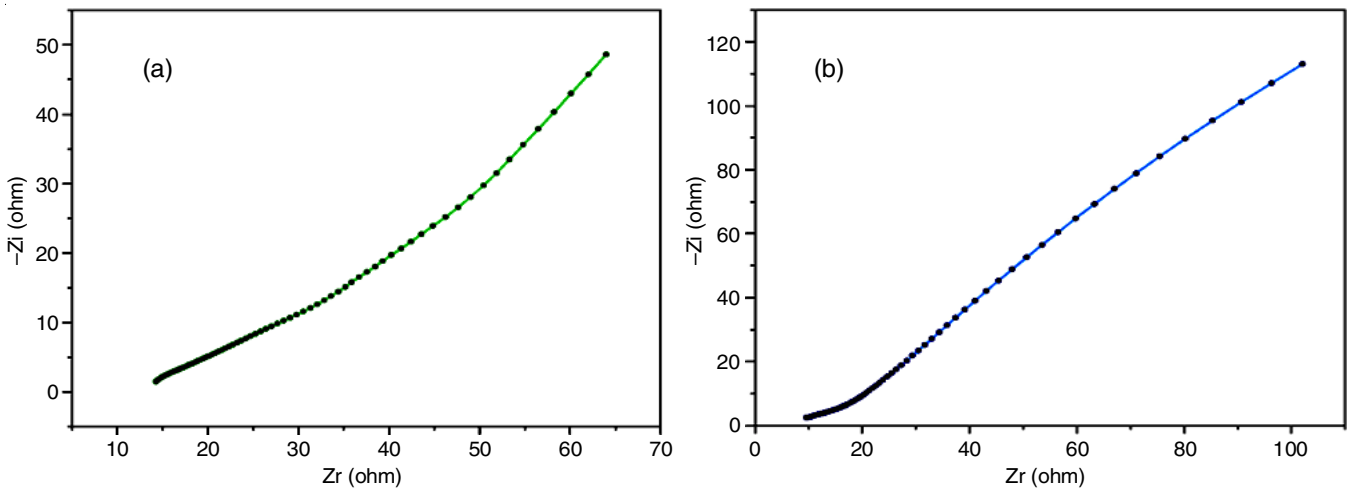

Fig. 8. Electrochemical impedance spectra of TCL-700 of the electrolyte (a) 1 M KOH and (b) 1 M H_2SO_4

TABLE-1
ELECTROCHEMICAL MEASUREMENTS OF TCL-700

Current density (μA)	Capacitance (F/g)		Scan rate (mV/s)		Capacitance (F/g)	
	KOH	H_2SO_4	KOH	H_2SO_4	KOH	H_2SO_4
250	54.4	21.63	10	10	112	186.5
200	73.6	28.46	20	20	38.4	228.7
125	238.8	32.42	30	30	27.4	188.9
100	68.48	28.46	40	40	23.6	171.9
75	238.8	21.63	50	50	20.9	148.7

asize the ease of synthesizing porous carbon from biowaste but also highlight its significant electrochemical performance, positioning it as a suitable candidate for scalable applications in electrochemical energy storage systems.

CONFLICT OF INTEREST

The authors declare that there is no conflict of interests regarding the publication of this article.

REFERENCES

1. S. Zhong, H. Zhu, L. Yang, X. Chi, W. Tan and W. Weng, *J. Mater. Chem. A Mater. Energy Sustain.*, **11**, 8101 (2023); https://doi.org/10.1039/D3TA00367A
2. J. Zhou, H. Xiao, W. Weng, D. Gu and W. Xiao, *J. Energy Chem.*, **50**, 280 (2020); https://doi.org/10.1016/j.jechem.2020.03.048
3. X. Chen, H. Zhao, J. Qu, D. Tang, Z. Zhao, H. Xie, D. Wang and H. Yin, *Green Chem.*, **22**, 7946 (2020); https://doi.org/10.1039/D0GC02626C
4. W. Weng, B. Jiang, Z. Wang and W. Xiao, *Sci. Adv.*, **6**, 9278 (2020); https://doi.org/10.1126/sciadv.aay9278
5. Y. Gogotsi, *ACS Nano*, **8**, 5369 (2014); https://doi.org/10.1021/nn503164x
6. G. Kothandam, G. Singh, X. Guan, J.M. Lee, K. Ramadass, S. Joseph, M. Benzigar, A. Karakoti, J. Yi, P. Kumar and A. Vinu, *Adv. Sci.*, **10**, 2301045 (2023); https://doi.org/10.1002/advs.202301045
7. W. Weng, S. Wang, W. Xiao and X.W.D. Lou, *Adv. Mater.*, **32**, 2001560 (2020); https://doi.org/10.1002/adma.202001560
8. T. Jiang, Y. Wang and G.Z. Chen, *Small Methods*, **7**, 2201724 (2023); https://doi.org/10.1002/smtd.202201724
9. A.T. Prasannakumar, R.R. Mohan, R. Rohith, V. Manju and S.J. Varma, *ChemistrySelect*, **8**, 202203564 (2023); https://doi.org/10.1002/slct.202203564
10. J. Hao, L. Yan, X. Zou, Y. Bai, Y. Han, C. Zhu, Y. Zhou and B. Xiang, *Small*, **19**, 2300467 (2023); https://doi.org/10.1002/smll.202300467
11. P. Simon, Y. Gogotsi and B. Dunn, *Science*, **343**, 1210 (2014); https://doi.org/10.1126/science.1249625
12. Z. Qiu, Z. Liu, X. Lu, S. Zhang, Y. Yan, C. Chi, C. Huangfu, G. Wang, P. Gao, W. Chi, Z. Xu, T. Wei and Z. Fan, *Small*, **19**, 2302316 (2023); https://doi.org/10.1002/smll.202302316
13. Y. Guan, Y. Cong, R. Zhao, K. Li, X. Li, H. Zhu, Q. Zhang, Z. Dong and N. Yang, *Small*, **19**, 2301276 (2023); https://doi.org/10.1002/smll.202301276
14. Q. Zhang, Y. He, G. Lin, X. Ma, Z. Xiao, D. Shi and Y. Yang, *J. Mater. Chem. A Mater. Energy Sustain.*, **9**, 10652 (2021); https://doi.org/10.1039/D1TA00302J
15. X. Li, W. Li, Q. Liu, S. Chen, L. Wang, F. Gao, G. Shao, Y. Tian, Z. Lin and W. Yang, *Adv. Funct. Mater.*, **31**, 2008901 (2021); https://doi.org/10.1002/adfm.202008901
16. J. Cao, J. Luo, P. Wang, X. Wang and W. Weng, *Mater. Technol.*, **35**, 522 (2020); https://doi.org/10.1080/10667857.2019.1699270
17. Y. Cheng, L. Wu, C. Fang, T. Li, J. Chen, M. Yang and Q. Zhang, *J. Mater. Res. Technol.*, **9**, 3261 (2020); https://doi.org/10.1016/j.jmrt.2020.01.022
18. C. Zhang, X. Liu, Z. Li, C. Zhang, Z. Chen, D. Pan and M. Wu, *Adv. Funct. Mater.*, **31**, 2101470 (2021); https://doi.org/10.1002/adfm.202101470
19. D. Cao, Q. Li, X. Sun, Y. Wang, X. Zhao, E. Cakmak, W. Liang, A. Anderson, S. Ozcan and H. Zhu, *Adv. Mater.*, **33**, 2105505 (2021); https://doi.org/10.1002/adma.202105505
20. Q. Li, D. Cao, M.T. Naik, Y. Pu, X. Sun, P. Luan, A.J. Ragauskas, T. Ji, Y. Zhao, F. Chen, Y. Zheng and H. Zhu, *ACS Sustain. Chem. Eng.*, **10**, 8704 (2022); https://doi.org/10.1021/acssuschemeng.2c00783

21. Q. Li, X. Sun, D. Cao, Y. Wang, P. Luan and H. Zhu, *Electrochem. Energy Rev.*, **5**, 18 (2022); https://doi.org/10.1007/s41918-022-00170-6
22. X. Sun, Q. Li, D. Cao, Y. Wang, A. Anderson and H. Zhu, *Small*, **18**, 2105678 (2022); https://doi.org/10.1002/smll.202105678
23. S.R.A. Sasono, M.F. Rois, W. Widiyastuti, T. Nurtono and H. Setyawan, *Results Eng.*, **18**, 101070 (2023); https://doi.org/10.1016/j.rineng.2023.101070
24. S.M. Omokafe, A.A. Adeniyi, E.O. Igbafen, S.R. Oke and P.A. Olubambi, *Int. J. Electrochem. Sci.*, **15**, 10854 (2020); https://doi.org/10.20964/2020.11.10
25. K.C. Lee, M.S.W. Lim, Z.Y. Hong, S. Chong, T.J. Tiong, G.T. Pan and C.M. Huang, *Energies*, **14**, 4546 (2021); https://doi.org/10.3390/en14154546
26. M.F.M. Yusop, E.M.J. Jaya, A.T. Mohd Din, O.S. Bello and M.A. Ahmad, *Chem. Eng. Technol.*, **45**, 1943 (2022); https://doi.org/10.1002/ceat.202200051
27. Z. Yang, G. Yan, X. Liu, Z. Feng, X. Zhu, Y. Mao, S. Chen, Z. Yu, R. Fan and L. Shan, *J. Renew. Mater.*, **10**, 3573 (2022); https://doi.org/10.32604/jrm.2022.022031
28. Y. Tan, Y. Ren, Z. Xu, Y. Zhu and H. Li, *J. Electron. Mater.*, **52**, 2603 (2023); https://doi.org/10.1007/s11664-023-10223-1
29. B. Shaku, T.P. Mofokeng, N.J. Coville, K.I. Ozoemena and M.S. Maubane-Nkadimeng, *Electrochim. Acta*, **442**, 141828 (2023); https://doi.org/10.1016/j.electacta.2023.141828
30. G. Dhakal, D. Mohapatra, Y.I. Kim, J. Lee, W.K. Kim and J.J. Shim, *Renew. Energy*, **189**, 587 (2022); https://doi.org/10.1016/j.renene.2022.01.105
31. P. Ozpinar, C. Dogan, H. Demiral, U. Morali, S. Erol, C. Samdan, D. Yildiz and I. Demiral, *Renew. Energy*, **189**, 535 (2022); https://doi.org/10.1016/j.renene.2022.02.126
32. X. Xu, K. Sielicki, J. Min, J. Li, C. Hao, X. Wen, X. Chen and E. Mijowska, *Renew. Energy*, **185**, 187 (2022); https://doi.org/10.1016/j.renene.2021.12.040
33. M. Biswal, A. Banerjee, M. Deo and S. Ogale, *Energy Environ. Sci.*, **6**, 1249 (2013); https://doi.org/10.1039/c3ee22325f
34. G. Byatarayappa, V. Guna, R.M. G, K. Venkatesh, Y. Zhao, N. N, N. Reddy and K. Nagaraju, *Sustain. Energy Fuels*, **6**, 4034 (2022); https://doi.org/10.1039/D2SE00802E
35. I. Kavya, D.S. Kumar, D. Sandhya, P. Janaki and M.C. Eswaraiah, *Indian J. Res. Pharm. Biotechnol.*, **3**, 410 (2015).
36. S.N. Kumar and N. Thampi, *J. Chem. Pharm. Res.*, **7**, 840 (2015).
37. N. Sudhan, K. Subramani, M. Karnan, N. Ilayaraja and M. Sathish, *Energy Fuels*, **31**, 977 (2017); https://doi.org/10.1021/acs.energyfuels.6b01829
38. X. Ma, H. Wang, Q. Wu, J. Zhang, D. Liang, S. Lu and Y. Xiang, *J. Electrochem. Soc.*, **166**, A236 (2019); https://doi.org/10.1149/2.0831902jes
39. N. Katagiri, N. Adachi and T. Ota, *J. Ceram. Soc. Jpn.*, **122**, 29 (2014); https://doi.org/10.2109/jcersj2.122.29
40. D. Wang, Y. Min and Y. Yu, *J. Solid State Electrochem.*, **19**, 577 (2015); https://doi.org/10.1007/s10008-014-2639-0
41. F. Giannazzo, R. Dagher, E. Schilirò, S.E. Panasci, F. Roccaforte, G. Greco, G. Nicotra,S. Agnello, J. Brault, Y. Cordier and A. Michon, *Nanotechnology*, **32**, 015705 (2021); https://doi.org/10.1088/1361-6528/abb72b
42. P. Divya and R. Rajalakshmi, *Mater. Today Proc.*, **27**, 44 (2020); https://doi.org/10.1016/j.matpr.2019.08.200
43. C. Pituello, O. Francioso, G. Simonetti, A. Pisi, A. Torreggiani, A. Berti and F. Morari, *J. Soils Sediments*, **15**, 792 (2015); https://doi.org/10.1007/s11368-014-0964-7
44. P. Fu, S. Hu, J. Xinag, L. Sun, T. Yang, A. Zhang, Yi Wang and G. Chen, 2009 International Conference on Energy and Environment Technology, Guilin, China, pp. 109-112 (2009); https://doi.org/10.1109/ICEET.2009.33
45. S. Suman and S. Gautam, *Energy Sources A Recovery Util. Environ. Effects*, **39**, 761 (2017); https://doi.org/10.1080/15567036.2016.1263252
46. S. Suman, D.S. Panwar and S. Gautam, *Energy Sources A Recovery Util. Environ. Effects*, **39**, 1007 (2017); https://doi.org/10.1080/15567036.2017.1283553
47. S. Tharani, *ECS Trans.*, **107**, 14433 (2022); https://doi.org/10.1149/10701.14433ecst
48. A. Khan, R. Arumugam Senthil, J. Pan, Y. Sun and X. Liu, *Batter. Supercaps*, **3**, 731 (2020); https://doi.org/10.1002/batt.202000046
49. S. Palanisamy, S.K. Kandasamy, S. Thangmuthu, D.K. Selvarasu, M. Panchanathan, P.V. Ramanai and B.S. Gevert, *J. Mater. Sci. Mater. Electron.*, **32**, 25175 (2021); https://doi.org/10.1007/s10854-021-06974-4